J. Fluid Mech. (2006), *vol.* 552, *pp.* 257–287.
doi:10.1017/S0022112006008652 Printed in the United Kingdom

Analysis of unsteady forces in ordered arrays of monodisperse spheres

By ANDREAS TEN CATE AND SANKARAN SUNDARESAN

Department of Chemical Engineering, Princeton University, Princeton, NJ 08544, USA

(Received 19 July 2004 and in revised form 12 October 2005)

Time-dependent flows of a Newtonian fluid through periodic arrays of spheres were simulated using the lattice-Boltzmann scheme. By applying a constant body force per unit mass to the fluid, a steady background fluid flow through the array of stationary spheres was first established. Subsequently, a small-amplitude perturbation to the body force, which varied periodically in time, was added and the long-time behaviour of the unsteady flow fields and the forces on the particles were determined. From the simulations, the pressure and friction (shear) forces acting on the particles were determined for a range of conditions. Results on simple cubic lattices are presented. Computations spanned a range of particle volume fractions ($0.1 < \phi < 0.4$), background flow Reynolds numbers ($0.25 \leqslant Re_p \leqslant 60$, where $Re_p = 2au_f/\nu$) and oscillatory flow Reynolds numbers ($0.9 \leqslant Re_\omega \leqslant 420$ with $Re_\omega = 2a^2\omega/\nu$). Here u_f is the superficial velocity of the fluid through the bed, a is the particle radius, ν is the kinematic viscosity of the fluid, and ω is the oscillation frequency.

In the limit of $Re_\omega \to 0$ the quasi-steady-state drag force was obtained. At low Re_p this force approached the steady-state drag force, while its increase with Re_p was stronger than the steady-state drag force, similar to that for isolated spheres given by Mei *et al.* (J. Fluid Mech., vol. 233, 1991, p. 613).

The unsteady force was decomposed into pressure and friction components. The phase angles of these components in the limit $Re_\omega \to \infty$ indicate that the virtual mass force contributes to the unsteady pressure force while the history force contributes to the friction force. The remainder of the unsteady friction and pressure forces is attributed to unsteady drag force.

The apparent virtual mass coefficient was found to vary from ~0.5 at high Re_ω, which is the well-known limit for isolated spheres in inviscid flows, to ~1.0 at low Re_ω. This change is clearly a consequence of viscous effects. The Re_ω at which the transition between these limits occurs increases with ϕ. The history force exhibits a strong decay towards lower values of Re_ω in accordance with the results of Mei *et al.* (1991) for isolated spheres; however, the Re_ω value at which this decay sets in increases appreciably with ϕ. This ϕ-dependence is associated with the limited separation between the particles available for the Stokes boundary layer.

It was found that the unsteady drag coefficient β' varies with Re_ω. At low Re_p, the drag coefficient initially decreases with increasing Re_ω, passes through a minimum and then increases strongly. With increasing Re_ω the relative contribution of pressure and friction forces to the unsteady drag force changes.

1. Introduction

Unsteady flows of suspensions are encountered in many applications in process industry. Gas–particle flows in bubbling fluidized beds, fast fluidized beds and

pneumatic transport lines, and liquid–solid flows in the turbulent processing of dense suspensions in crystallization and precipitation processes are common examples. The scale of industrial process equipment is typically in the range of 1–10 m and is usually orders of magnitude larger than the scale of the solid particles (1–1000 μm). In these applications, typical frequencies that characterize the transient behaviour may vary from 0.1–1 Hz for fluidized beds, to 1–100 Hz for agitated turbulent suspensions.

Flows of fluid–particle suspensions in such processes are commonly modelled via the (spatially or ensemble) averaged two-fluid equations (see e.g. Jackson 2000):

$$\frac{\partial \rho_s \phi}{\partial t} + \nabla \cdot (\rho_s \phi \boldsymbol{u}_s) = 0, \tag{1.1}$$

$$\frac{\partial \rho_f (1-\phi)}{\partial t} + \nabla \cdot (\rho_f (1-\phi) \boldsymbol{u}_f) = 0, \tag{1.2}$$

$$\rho_s \phi \left[\frac{\partial \boldsymbol{u}_s}{\partial t} + \boldsymbol{u}_s \cdot \nabla \boldsymbol{u}_s \right] = \phi \nabla \cdot \boldsymbol{\Pi}_f + \nabla \cdot \boldsymbol{\Pi}_s + \boldsymbol{F} + \phi \rho_s \boldsymbol{g}, \tag{1.3}$$

$$\rho_f (1-\phi) \left[\frac{\partial \boldsymbol{u}_f}{\partial t} + \boldsymbol{u}_f \cdot \nabla \boldsymbol{u}_f \right] = (1-\phi) \nabla \cdot \boldsymbol{\Pi}_f - \boldsymbol{F} + (1-\phi) \rho_f \boldsymbol{g}, \tag{1.4}$$

where the two phases are treated as interpenetrating continua; ρ_s and ρ_f are the densities of the particles and the fluid, respectively; $\boldsymbol{u}_s$ and $\boldsymbol{u}_f$ are the local-average particle- and fluid-phase velocities, respectively; and ϕ is the volume fraction of the particle phase. $\boldsymbol{\Pi}_s$ and $\boldsymbol{\Pi}_f$ are the effective particle- and fluid-phase stress tensors, while $\boldsymbol{F}$ is the hydrodynamic interaction force between the particle and fluid phases. These equations are completed with closure relations for the particle- and fluid-phase stress tensors and the hydrodynamic forces in terms of the local particle volume fraction, rates of deformation of the two phases, etc.

A principal component of the hydrodynamic force $\boldsymbol{F}$ is the drag force $\boldsymbol{F}_d$. For a single particle in steady motion, the dependence of the drag force on particle Reynolds number is given by the well-known drag curve that relates the drag coefficient to the steady particle Reynolds number (e.g. Clift, Grace & Weber 1978). In two-fluid modelling approaches, the drag force is usually expressed as

$$\boldsymbol{F}_d = -\beta (\boldsymbol{u}_s - \boldsymbol{u}_f), \tag{1.5}$$

where $\boldsymbol{F}_d$ gives the drag force per unit volume of mixture. The effective drag coefficient, β, depends on particle size, fluid viscosity and density, particle-phase volume fraction and the local relative velocity between the phases. A number of different expressions have been proposed in the literature for β, which have been summarized by Li & Kuipers (2003).

With unsteady flow, additional contributions arise due to the instantaneous accelerations of the phases and due to the history of the acceleration. For a single particle in unsteady Stokes flow the virtual (or added) mass force

$$\widehat{\boldsymbol{F}}_v = -\frac{1}{2} \frac{4}{3} \pi a^3 \rho_f \frac{\mathrm{d}(\boldsymbol{v}_p - \boldsymbol{u}_\infty)}{\mathrm{d}t}, \tag{1.6}$$

and history (or Basset) force

$$\widehat{\boldsymbol{F}}_h = -6a^2 \sqrt{\pi \rho_f \mu} \int_{-\infty}^{t} \left[\frac{\mathrm{d}(\boldsymbol{v}_p - \boldsymbol{u}_\infty)}{\mathrm{d}\tau} \right] \frac{1}{\sqrt{t-\tau}} \, \mathrm{d}\tau \tag{1.7}$$

are the familiar analytically obtained unsteady forces (see e.g. Basset 1888; Landau & Lifshitz 1978; Clift *et al.* 1978; Crowe, Sommerfeld & Tsuji 1997). The particle

velocity is expressed as $\boldsymbol{v}_p$ and $\boldsymbol{u}_\infty$ indicates the undisturbed velocity of the fluid far away from the particle while $\widehat{\cdot}$ indicates that the force acts on a single sphere.

The virtual mass and history forces acting on a single particle have been studied by a number of authors. One of the first experimental studies on this subject was done by Odar & Hamilton (1964), who measured the force acting on a submerged sphere, undergoing rectilinear oscillating motion. The total force measured was partitioned into three contributions: quasi-steady drag force, virtual mass force and history force, where the first was described with a drag coefficient obtained from a drag curve. The virtual mass and history forces were parameterized by replacing the factor $1/2$ on the right-hand side of (1.6) with a virtual mass coefficient f_v and multiplying the right-hand side of (1.7) with a history coefficient f_h. The dependence of these coefficients on the experimental conditions was then determined, and correlated in terms of the instantaneous acceleration number (Odar & Hamilton 1966). This correlation has been mentioned and used by many authors (e.g. Schöneborn 1975; Clift *et al.* 1978; Crowe *et al.* 1997).

Mei, Lawrence & Adrian (1991) computed unsteady forces on an isolated sphere in the presence of small-amplitude fluctuations in the free-stream velocity. They found that, in the low-frequency limit, the long time decay of the history force varied as t^{-2}, which is different from the $t^{-1/2}$ behaviour in Basset's result. Based on this result, Mei & Adrian (1992) devised a kernel that interpolated between the short-time and the long-time behaviour of the history force. In these studies it was further observed that the virtual mass coefficient was practically constant at 0.5, in contrast to Odar & Hamilton (1964). Mei (1994) demonstrated that the correlation of Odar & Hamilton (1966) did not make any physical sense and that the alternative correlation with the adapted kernel formulation predicted the total force on the particle rather accurately.

In the numerical studies of Rivero, Magnaudet & Fabre (1991) and Chang & Maxey (1994), the force on a particle was partitioned into two parts: one arising from the action of the non-uniform pressure distribution and other due to the shear (friction) stresses. The virtual mass force was attributed to an instantaneous increase in the pressure component and values for the virtual mass coefficient of approximately 0.5 were obtained. Chang & Maxey (1995) have also addressed the virtual mass force in a study of linear accelerative fluid motion, finding once again values of approximately 0.5. The decay of the friction force over time was compared to the decay of the history force; for short times it was found to agree well with the decay of $t^{-1/2}$ while at longer times a steeper decay was found, in agreement with the results of Mei & Adrian (1992). The influence of history forces on the trajectory of a single particle at intermediate Reynolds numbers has been addressed by Kim, Elghobashi & Sirignano (1998), who extended the formulation of the history kernel as proposed by Mei & Adrian (1992). The effect of spatial inhomogeneity of the flow field on unsteady forces acting on a single sphere was recently studied numerically by Bagchi & Balachandar (2003).

Lovalenti & Brady (1993*a*) used the general reciprocal theorem for the Navier–Stokes equations to derive an expression, accurate to $O(Re)$, for the unsteady force acting on an isolated sphere in a uniform flow, exposed to arbitrary acceleratory motion. This expression was then applied to analyse small-amplitude oscillatory motion of the free-stream velocity (Lovalenti & Brady 1993*b*) The predicted unsteady force agreed well with that obtained by Mei *et al.* (1991) for $Re_p \approx 0.5$. In contrast to the algebraic decay proposed by Mei & Adrian (1992), Lovalenti & Brady (1993*b*) found that the integration kernel for the history force decays exponentially.

In the above studies, the dynamic forces were evaluated for an isolated sphere. However, the assumption that the flow field is not disturbed by other particles only

holds for dilute suspensions. The two main points that alter the description of the unsteady forces in dense suspensions compared to the dilute or single-particle case are (i) the representation of the relative velocity and (ii) the influence of the hydrodynamic interaction between particles at close proximity in unsteady flow.

The relative velocity used in the virtual mass and history force expressions ((1.6) and (1.7)) is given by the difference between the particle velocity and the fluid velocity, undisturbed by the presence of the particle. In modelling two-phase flow of dense suspensions, the instantaneous velocity of each phase is determined from the average over a local domain that is larger than the individual particles but smaller than the large scales of the flow. The relative velocity and acceleration are therefore limited to the scale over which averaging is applied and the fluid velocity is not the undisturbed velocity, which will alter the expressions for the force and may also influence the values of the virtual mass and history coefficients.

The arrangement of the particles will alter the interstitial flow pattern. A steadily oscillating particle with a no-slip boundary will develop a Stokes boundary layer. The approximate thickness of this boundary layer, δ, is $\sqrt{2\nu/\omega}$ (Landau & Lifshitz 1978). In moderate- to high-density suspensions the dimensions of the boundary layer can easily become comparable to the separation between the particles and hydrodynamic particle–particle interactions will affect the unsteady forces.

A number of authors have addressed the virtual mass and history forces in dense suspensions of particles or bubbles (Zuber 1964; Biesheuvel & Spoelstra 1989; Felderhof 1991; Sangani, Zhang & Prosperetti 1991). In these studies unsteady motion is limited to the high-frequency regime. This assumption ensures that the Stokes boundary layers remain closely attached to the surface of the particles and modification of the unsteady forces due to the overlap of the Stokes boundary layers is not accounted for.

The objective of the present study is to investigate numerically the behaviour of unsteady forces in regular arrays (simple cubic lattice, SCL and face-centred cubic, FCC) of spheres over a range of Reynolds numbers, volume fractions and unsteady flow conditions. For solution of the Navier–Stokes equations we use a lattice-Boltzmann scheme. The use of a numerical approach lifts the limitation of sampling only the high-frequency regime. We study the dynamic forces in a field driven by an oscillating body force which includes a constant mean part to generate the background flow.

Studies on steady drag forces in periodic arrays of particles are widely available in the literature. Variation of drag force with solids volume fraction at low Reynolds numbers has been reported by Hasimoto (1959) and Sangani & Acrivos (1982). More recently, numerical studies of steady drag force at a wider range of Reynolds numbers have also appeared (Hill, Koch & Ladd 2001*a*, *b*; Kandhai, Derksen & Van den Akker 2003). These authors have employed the lattice-Boltzmann method to simulate the flow and have obtained data on the flow field and drag force in different geometries (i.e. SCL, FCC and random periodic arrays) over a wide range of Reynolds numbers and solids volume fraction. In the current study we apply the same method as these authors, and extend the analysis to unsteady forces.

The decay of the history force towards the low-frequency limit was attributed to the advection terms in the Navier–Stokes equations, which become important when the Oseen length scale, $\ell = a/Re_p$, and the Stokes boundary layer thickness δ become comparable (Mei *et al.* 1991). In periodic arrays of particles the separation between neighbouring particles introduces an additional length scale. At low Reynolds numbers this separation can easily be smaller than the Oseen length, and therefore will change the character of the unsteady force. In our analysis we will examine

the behaviour of the unsteady force over a wide range of Re_ω at different volume fractions ϕ and particle Reynolds number to investigate this effect, and demonstrate that both parameters have a distinct impact on the unsteady forces.

In § 2 we describe the basis of our simulation method and the manner in which the unsteady forces on the sphere are determined. In this section some results on steady forces are also presented, which are essential before one can embark on a study of the dynamic forces. In §§ 3 and 4, we present results on unsteady flow fields and forces, respectively. As the transient calculations require long simulation times, we rely on simulation of a single particle in an SCL arrangement, which is computationally less demanding, to probe in detail the various aspects of the oscillating flow. In § 5 we summarize our main results.

2. Approach

2.1. *Oscillatory flow*

We study the force acting on a stationary sphere in a cubic, fully periodic domain. The motion of an incompressible, Newtonian fluid with a constant viscosity through the interstitial region between the particles is described by the continuity equation

$$\nabla \cdot \boldsymbol{u}^* = 0 \tag{2.1}$$

and the Navier–Stokes equations,

$$\frac{\partial \boldsymbol{u}^*}{\partial t^*} + \boldsymbol{u}^* \cdot \nabla \boldsymbol{u}^* = -\frac{\nabla p^*}{\rho_f} + \nu \nabla^2 \boldsymbol{u}^* + \boldsymbol{g}^* \tag{2.2}$$

where $\boldsymbol{u}$ is the fluid velocity, ν the fluid kinematic viscosity, ρ_f the fluid density, p the pressure and $\boldsymbol{g}$ the body force per unit mass that is used to drive the flow in our simulations. The $*$ is used to denote dimensional quantities.

The flow in a periodic unit cell is characterized by the volume-averaged velocity. The interstitial velocity refers to the mean fluid velocity obtained by averaging the velocity over the volume of fluid in a unit cell, and is denoted with subscript f as u_f^*. In the literature (e.g. Hasimoto 1959; Sangani & Acrivos 1982; Hill *et al.* 2001*a*), results are often presented in terms of the superficial velocity, which is obtained by averaging the velocity of each phase over the entire volume of a unit cell. Where used, superficial velocities will be denoted in this paper by angle brackets as in $\langle u^* \rangle$. Superficial and interstitial velocity are related as $\langle u^* \rangle = (1-\phi) u_f^*$.

Unsteady conditions are obtained by superimposing an oscillation with a scaled amplitude α and frequency ω^* onto the body force,

$$g^* = g_0^*(1.0 + \alpha \sin(\omega^* t^*)) \tag{2.3}$$

where g^* is the magnitude of the body force per unit mass. Generally a small amplitude α is chosen such that the response amplitude of the fluid velocity remains small and the variation of the unsteady forces in response to the fluctuating flow field remains linear. The magnitude of the interstitial velocity in the steady oscillating state, u_f^*, can be written as

$$u_f^* = \bar{u}_f^* + u_f'^* = u_{f,0}^*(1.0 + \alpha_u \sin(\omega^* t^* + \theta_u)) \tag{2.4}$$

where $\bar{u}_f^*$ is the time-averaged interstitial fluid velocity, $u_f'^*$ the fluctuating velocity, and α_u and θ_u are the scaled response amplitude and the phase angle.

By decomposing the flow field into a mean and a fluctuating part with small amplitude α_u, we can rewrite the Navier–Stokes equations in terms of these parts. The

equations can be made dimensionless by scaling the length scales with the particle radius a^*, scaling the velocities with the mean velocity $u^*_{f,0}$ and scaling the time in the transient terms with $1/\omega^*$. In this way, the velocity is scaled as $u = u^*/u^*_{f,0}$. The dimensionless acceleration is scaled as $g_0 = g^*_0 a^*/u^{*2}_{f,0}$. Further, pressure also can be separated into a mean and a fluctuating part and is made dimensionless via $p = \bar{p} + p' = p^*/(\rho^*_f u^{*2}_{f,0})$.

Separating the steady part of order 1 from the unsteady part of order α_u we obtain

$$\bar{\boldsymbol{u}} \cdot \nabla \bar{\boldsymbol{u}} = -\nabla \bar{p} + \frac{2}{Re_p} \nabla^2 \bar{\boldsymbol{u}} + \boldsymbol{g}_0 \tag{2.5}$$

for the steady background flow, and

$$Sl \frac{\partial \boldsymbol{u}'}{\partial t} + \bar{\boldsymbol{u}} \cdot \nabla \boldsymbol{u}' + \boldsymbol{u}' \cdot \nabla \bar{\boldsymbol{u}} = -\nabla p' + \frac{2}{Re_p} \nabla^2 \boldsymbol{u}' + \boldsymbol{g}_0 \alpha \sin(t) \tag{2.6}$$

for the unsteady part. In (2.6) all terms are of order α, hence the appearance of α in the body force term, while the term $\boldsymbol{u}' \cdot \nabla \boldsymbol{u}'$ is of higher order and has been dropped.

The unsteady flow equation is characterized by two dimensionless groups, the Strouhal number $Sl = a^* \omega^*/u^*_{f,0}$, and the particle Reynolds number $Re_p = 2a^* u^*_{f,0}/\nu^*$. The oscillation Reynolds number is defined as $Re_\omega = Re_p Sl = 2a^{*2}\omega^*/\nu^*$. The Stokes flow result obtained by Basset applies only for $Re_p \ll 1$, $Sl \gg 1$ and $Re_\omega \gg 1$.

2.2. *Unsteady forces*

Before we proceed further, let us first examine the relationship between the virtual mass and history forces per unit volume of the fluid–particle mixture, $\boldsymbol{F}_v$ and $\boldsymbol{F}_h$, respectively, as they should enter in (1.3) and (1.4), and the corresponding forces $\widehat{\boldsymbol{F}}_v$ and $\widehat{\boldsymbol{F}}_h$ per particle in the mixture. (In this section, we present all the quantities in dimensional form for the sake of convenience, but will resume presentation of all quantities in dimensionless form subsequently.) One can eliminate $\nabla \cdot \boldsymbol{\Pi}_f$ between (1.3) and (1.4) to obtain

$$m_p \left[\frac{\partial \boldsymbol{u}_s}{\partial t} + \boldsymbol{u}_s \cdot \nabla \boldsymbol{u}_s \right] = m_p \boldsymbol{g} + m_f \left[\left(\frac{\partial \boldsymbol{u}_f}{\partial t} + \boldsymbol{u}_f \cdot \nabla \boldsymbol{u}_f \right) - \boldsymbol{g} \right] + \frac{1}{n} \nabla \cdot \boldsymbol{\Pi}_s + \frac{\boldsymbol{F}}{n(1-\phi)} \tag{2.7}$$

where n is the number density of particles, m_p is the mass of a single particle and m_f is the mass of fluid displaced by a particle. This reveals that a natural way to write $\boldsymbol{F}_v$ and $\boldsymbol{F}_h$ in the two-fluid model is

$$\boldsymbol{F}_v = n(1-\phi)\widehat{\boldsymbol{F}}_v, \quad \boldsymbol{F}_h = n(1-\phi)\widehat{\boldsymbol{F}}_h. \tag{2.8}$$

As we employ spatially periodic unit cells, the flow quantities obtained by averaging over the unit cell are spatially uniform (from one cell to the next). Therefore, in our calculations, the particle volume fraction remains homogeneous and independent of time, while $\boldsymbol{u}_s$ and $\boldsymbol{u}_f$ (in the two-fluid model) depend only on time. In view of this, and (1.6), (1.7) and (2.8), we write

$$\boldsymbol{F}_v = -\rho_f \phi (1-\phi) f_v \left[\frac{\partial \boldsymbol{u}_s}{\partial t} - \frac{\partial \boldsymbol{u}_f}{\partial t} \right] \tag{2.9}$$

and the history force per unit volume of the mixture, $\boldsymbol{F}_h$, takes the form

$$\boldsymbol{F}_h = -\frac{9}{2a} \sqrt{\frac{\rho_f \mu}{\pi}} \phi (1-\phi) f_h \int_{-\infty}^{t} \left[\frac{\partial \boldsymbol{u}_s}{\partial t} - \frac{\partial \boldsymbol{u}_f}{\partial t} \right] \frac{1}{\sqrt{t-\tau}} \, \mathrm{d}\tau. \tag{2.10}$$

These equations give a generalized description of the virtual mass and history forces, where the dependence of the forces on local conditions is captured by the parameters f_v and f_h.

From our fluid flow simulations, we obtain a time series of the force on the particle. If the flow remains in the linear response regime, then the force on the particle can also be decomposed into a steady part and a fluctuating part (analogous to the interstitial fluid velocity), which gives

$$\boldsymbol{F} = \bar{\boldsymbol{F}} + \boldsymbol{F}', \tag{2.11}$$

where the steady part $\bar{\boldsymbol{F}}$ can be described by the drag relation (1.5) as

$$\bar{\boldsymbol{F}}_d = \beta \boldsymbol{u}_{f,0}. \tag{2.12}$$

Since our simulations are carried out with stationary particles, we drop the solid-phase velocity $\boldsymbol{u}_s$ in our analysis below. It is understood that the fluid velocities are measured relative to the particles. We will examine how $\boldsymbol{F}'$ should be partitioned into unsteady drag, virtual mass and history forces.

2.3. *The lattice-Boltzmann simulation setup*

The lattice-Boltzmann method, used in the present study, is an efficient numerical scheme to simulate fluid flow on a cubic lattice. The fluid motion is mimicked by a distribution of mass ρ_i^* that propagates at discrete time steps in M discrete directions i on a cubic grid. By applying mass and momentum conserving collision rules and low-Mach-number conditions, the flow simulated by the lattice-Boltzmann scheme obeys the incompressible Navier–Stokes equations (for more details see e.g. Chen & Doolen 1998, Rothman & Zaleski 1997, Succi 2001 or Chopard & Droz 1998). The lattice-Boltzmann scheme used in this work is based on the commonly used single relaxation time BGK scheme with 19 velocity directions (D3Q19, Qian, d'Humieres & Lallemand 1992).

The unsteady flow is studied by full three-dimensional simulation of the flow around a steady sphere in a fully periodic domain with no-slip boundary conditions at the sphere surface. As no-slip boundary condition the bounce-back rule was used, identical to the method described by Ladd (1994). This method assumes that the boundary is positioned halfway on the link between two grid nodes, indicated by the filled squares in figure 1.

The hydrodynamic forces that act on the sphere surface are computed via the bounce-back rule. With this method, mass that is about to propagate into the sphere is reflected back into the fluid. The total force is computed as the sum of the momentum change over the entire surface, which for a steady sphere can be written as

$$\boldsymbol{F}^* = \sum_{n_l} f_i^* = \sum_{n_l} \Delta\rho_i^* c_i^* \tag{2.13}$$

where $\boldsymbol{c}_i^*$ is the discrete velocity at which the mass ρ_i^* propagates in lattice-direction i, while the summation is taken over all the n_l links that are cut by the sphere surface.

For the analysis of the unsteady forces we are interested in a decomposition of the total hydrodynamic force into pressure and friction components. To determine these components from the lattice-Boltzmann simulations the force calculations of the bounce-back method were extended. Using the outward normal at the location of the boundary node and the momentum vector $\boldsymbol{f}_i^*$, two supporting normal vectors

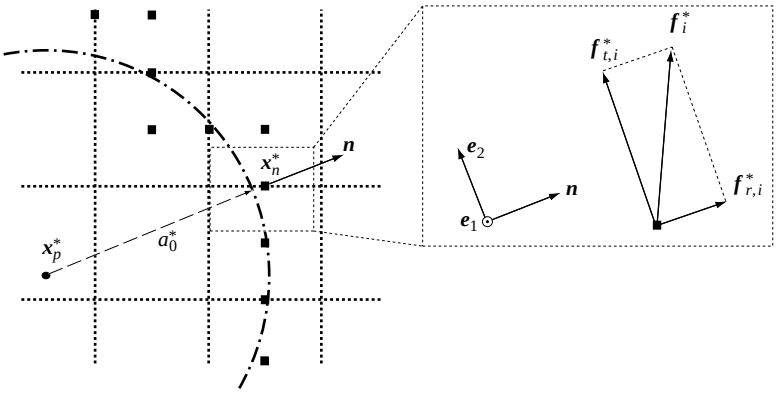

FIGURE 1. The geometry of a sphere of radius a_0^* on a cubic grid. The grid nodes of the lattice-Boltzmann scheme are located at the intersection of the grid lines (dotted lines). The sphere centre is indicated by $\boldsymbol{x}_p^*$ and the bounce-back node (■) by $\boldsymbol{x}_n^*$. The outward unit normal vector $\boldsymbol{n}$ and the two supporting unit vectors $\boldsymbol{e}_1$ and $\boldsymbol{e}_2$ at the bounce-back node are used to decompose the force contribution $\boldsymbol{f}_i^*$ at each link into a radial component $\boldsymbol{f}_{r,i}^*$ and a tangential component $\boldsymbol{f}_{t,i}^*$.

were determined,

$$\boldsymbol{e}_1 = \frac{\boldsymbol{f}_i^* \times \boldsymbol{n}}{|\boldsymbol{f}_i^* \times \boldsymbol{n}|}, \qquad \boldsymbol{e}_2 = \boldsymbol{n} \times \boldsymbol{e}_1, \tag{2.14}$$

via which the radial and tangential components were calculated as

$$\boldsymbol{f}_{r,i}^* = (\boldsymbol{f}_i^* \cdot \boldsymbol{n})\boldsymbol{n}, \qquad \boldsymbol{f}_{t,i}^* = (\boldsymbol{f}_i^* \cdot \boldsymbol{e}_2)\boldsymbol{e}_2. \tag{2.15}$$

Summation of thsese components over all boundary links gives the pressure and friction force, i.e. $\widehat{\boldsymbol{F}}_p = \sum \boldsymbol{f}_{r,i}$ and $\widehat{\boldsymbol{F}}_f = \sum \boldsymbol{f}_{t,i}$.

Since the spherical shape of the object is approximated by a staircase-shaped boundary condition in a cubic domain, a small correction to the sphere size is usually applied. The correction used in this paper follows the same procedure as Hill *et al.* (2001*a*). For a sphere with a given input radius, a_0^*, an effective hydrodynamic radius, a^*, can be determined using an analytic drag relation for a single sphere in a periodic array (Hasimoto 1959; Sangani & Acrivos 1982). The hydrodynamic radius is dependent on the kinematic viscosity used in the simulations. When we apply a kinematic viscosity of $\nu^* = 0.01(\Delta x^{2^*}/\Delta t^*)$, we find, similar to Hill *et al.* (2001*a*), $a^* \simeq (j + 0.8)\Delta x^*$ for $a_0^* = (j + 0.5)\Delta x^*$, where j indicates the integer value for the sphere radius (i.e. $j = 1, 2 \ldots \Delta x^*$ corresponds to $a_0^* = 1.5, 2.5 \ldots \Delta x^*$ and $a^* = 1.8, 2.8 \ldots \Delta x^*$). The correction is generally small in our simulations, as we use high resolution on the sphere geometry (typically $a_0^* \geqslant 12.5\Delta x^*$). Here Δx^* indicates the grid spacing and Δt^* indicates the timestep of the simulation. In lattice-Boltzmann simulations these are typically chosen as 1. In the present work this was also the case. Therefore, unit measures are dropped when properties are discussed, indicating that $\Delta x^* = 1$ and $\Delta t^* = 1$ are implied.

The dimensionless flow variables that determine the conditions of our simulation are the volume fraction $\phi = n_p \frac{4}{3}\pi a^{*3}/L^{*3}$, with n_p the number of spheres in the domain and L^* the length of the sides of a cubic domain, the particle Reynolds number $Re_p = 2a^* u_{f,0}^*/\nu^*$ and the unsteady Reynolds number $Re_\omega = 2a^{*2}\omega^*/\nu^*$. The following considerations were taken into account when setting the dimensional

lattice-Boltzmann parameters to obtain the desired dimensionless parameters in our simulations:

(i) $u^*_{f,0}$ is chosen much smaller than the speed of sound, $c_s = \sqrt{1/3}$. Its value was determined according to the desired Reynolds number, after ν^* and a were set. The flow is driven by the body force g^*_0. During an initialization period a proportional-differential (PD) control scheme is used (Stephanopoulos 1984) to steer the fluid velocity to its desired value by adjusting the body force proportionally to the deviation $\delta u^*(t^*) = u^*_{f,0}(t^*) - u^*_{f,0set}$ and proportionally to the temporal derivative $\mathrm{d}\delta u^*/\mathrm{d}t^*$.

(ii) ν^*, the kinematic viscosity in lattice-Boltzmann units, is chosen in the range $0.01 \leqslant \nu^* \leqslant 0.1$. At smaller Reynolds numbers larger ν^* values are chosen, to permit larger velocities $u^*_{f,0}$.

(iii) $\omega^* = 2\pi/\tau^*$ is set via the oscillation time τ^*. As rule of thumb to achieve good (temporal and spatial) resolution at least $\tau^* \geqslant 1000$ was chosen. The smallest spatial structures in the oscillating flow field are the Stokes boundary layers, whose dimension can be estimated by $\delta \sim a\sqrt{4/Re_\omega} = \sqrt{\nu^*\tau^*/\pi}$. This shows that the spatial resolution of the smallest scales in the flow is determined only by the viscosity and the oscillation time scale. It was ensured that at the highest frequencies a resolution of at least four gridpoints is maintained in the boundary layer. Since the choice of τ^* is limited, to achieve high values of Re_ω at a given τ^* and ν^*, large sphere radii are required.

(iv) α, the forcing amplitude, was chosen in the range $0.01 \leqslant \alpha \leqslant 0.25$. At high frequencies the response amplitudes of the velocity and forces, see following sections, are much smaller than at low frequencies. Therefore α was adjusted with ω to obtain small but substantial response amplitudes.

(v) a_0 participates in all three dimensionless flow variables. Its value was chosen such that sufficient spatial resolution was obtained across the smallest separation between neighbour spheres, and such that a desired maximum value of Re_ω could be obtained. After ν^* was set, a calibration run was done to determine the corresponding hydrodynamic radius a.

(vi) L^* was set to obtain a desired ϕ.

There was not a specific procedure by which the parameters were determined, but rather the values were chosen while keeping the above guidelines in mind. When simulation results appeared to be sensitive to e.g. spatial or temporal resolution, simulations at increased resolution were done to determine whether numerical convergence was achieved.

2.4. *Steady drag forces*

In figure 2(*a*), the drag force under creeping flow is compared to the polynomial result of Sangani & Acrivos (1982), which is an extension to Hasimoto (1959), to describe the drag force up to higher volume fractions. Hasimoto (1959) originally calculated the force on the sphere in periodic arrays as the sum of drag and buoyancy force. Consequently, the force plotted in the figure is given accordingly,

$$K = \frac{\widehat{F}^*}{\widehat{F}^*_{St}} = \frac{\widehat{F}^*_d + \widehat{F}^*_b}{6\pi\mu^* a^* |\langle u^* \rangle|}, \tag{2.16}$$

where the Stokes drag, based on $\langle u^* \rangle$, is used to normalize the force. The vector notation is dropped since only flow directed along one of the principal axes of the periodic cell is being considered. The buoyancy force is obtained from the simulations as $\widehat{F}^*_b = v^*_p \rho^*_f g^*_0$, with v^*_p being the particle volume. It is clear that our simulations capture the analytical expression for the drag force accurately. Figure 2(*b*) demonstrates the

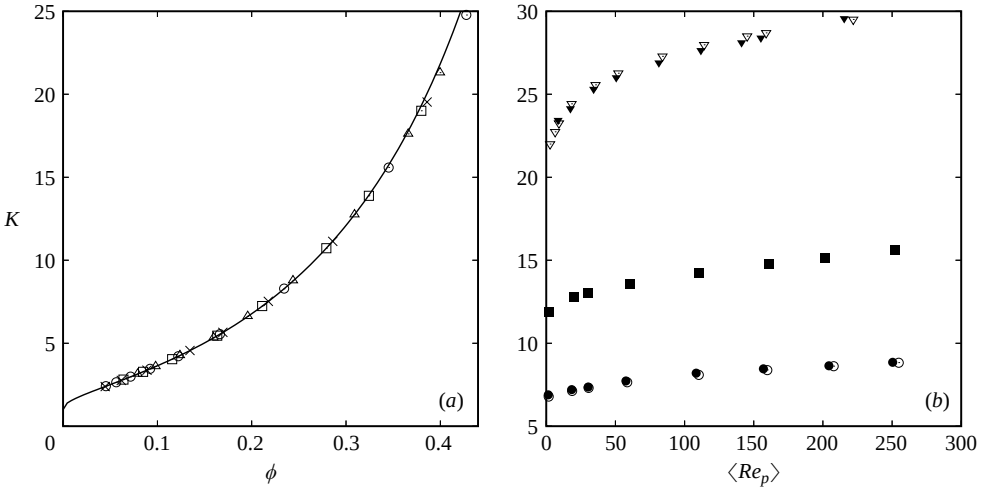

FIGURE 2. Steady drag force on a sphere in an SCL array. (*a*) Comparison between lattice–Boltzmann simulations and the polynomial result of Sangani & Acrivos (1982) at Stokes flow conditions ($a_0^* = 8.5$ (×), $a_0^* = 12.5$ (○), $a_0^* = 16.5$ (□), $a_0^* = 30.5$ (△)); (*b*) drag force versus $\langle Re_p \rangle$ at $\phi = 0.20$ (●, ○), $\phi = 0.30$ (■), $\phi = 0.40$ (▼, ▽). Excellent agreement is obtained with the resuls extracted from Hill *et al.* (2001 *b*), figures 10 and 13, marked with the open symbols. Re_p based on $\langle u^* \rangle$.

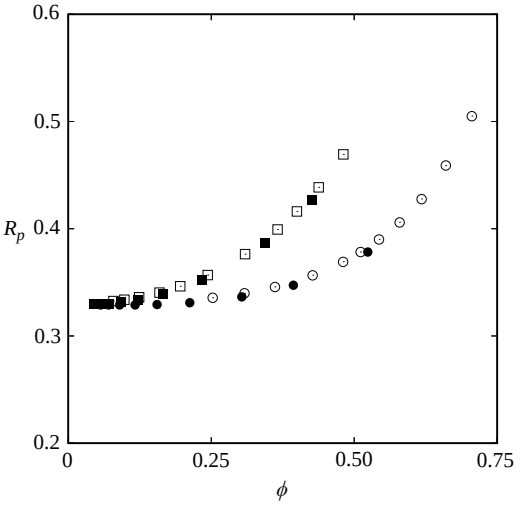

FIGURE 3. Variation of R_p with ϕ for an SCL and FCC type geometry at $Re_p = 0.1$. (SCL: ■, $a = 12.7$; □, $a = 30.7$; FCC: ●, $a = 12.7$; ○, $a = 30.7$).

behaviour of the dimensionless drag force with varying Reynolds number and volume fraction. The trends are in excellent agreement with the results of Hill *et al.* (2001 *b*).

In figure 3 the partitioning of the hydrodynamic force (i.e. the drag force $\widehat{F}_d^*$) into pressure and friction components is shown. The ratio of the pressure component to the total drag force is characterized by

$$R_p = \frac{\widehat{F}_p^*}{\widehat{F}_d^*}. \tag{2.17}$$

This parameter is used throughout this paper to indicate the ratio of the pressure force to the sum of pressure and friction forces under steady flow conditions.

For low-Reynolds-number flows, the variation of R_p with volume fraction is given in figure 3 for both the SCL and the FCC geometry. It is well known that for Stokes flow around an isolated sphere, the ratio R_p is exactly 1/3. The figure shows that in the limit $\phi \to 0$, this value is approached in both geometries. In the case of the FCC geometry, the increase starts at a higher volume fraction. The ratio exceeds 0.5 as ϕ approaches its maximum value (SCL, $\phi_{max} = \pi/6$, FCC $\phi_{max} = \sqrt{2}\pi/6$). This strong increase arises because at high volume fractions the fluid motion is forced through specific pathways between the particles. Such channelling, which for SCL is of a different nature than for FCC, decreases the contribution of frictional traction on the particles.

For the simulations presented in this paper, a validation of the unsteady force and flow field as a function of Re_ω is relevant. For unsteady flow about a sphere there is no analytical solution for comparison. However, for the case of pulsatile channel flow, validation of the lattice-Boltzmann method against an analytical flow profile is available and has been presented by Artoli, Hoekstra & Sloot (2002). Their results show that the lattice-Boltzmann method is capable of capturing the unsteady flow profile even at moderate to low resolution. Identical test cases were run and reproduced their result. For reasons of conciseness these data are not presented. The interested reader is referred to Artoli *et al.* (2002). With the requirement that at least four gridpoints are placed in the boundary layer region, sufficient resolution is warranted to ensure an accurate representation of the unsteady flow field.

3. The unsteady flow field

3.1. *The SCL geometry at low Reynolds number*

Figure 4 presents the temporal variation of the streamwise velocity component (u_x) along the line perpendicular to the flow direction, joining the centres of two neighbouring particles. Figure 4(*a*) ($Re_\omega = 25$) shows u_x profiles at six different times within one-half of an oscillation cycle. It is readily apparent that the velocity profile is nearly parabolic and that the fluctuations about the mean are very small. Profiles of the fluctuating part of the streamwise velocity (u'_x) at these six times are shown in figures 4(*b*)–4(*d*) for three different values of Re_ω. These figures present the fluctuating velocity over half a time cycle from maximum negative amplitude to maximum positive amplitude, with the time proceeding in the upward direction.

Figure 4(*b*) ($Re_\omega = 206$) shows a profile that is characteristic for an oscillating flow along a solid wall or inside a channel. The most responsive part of the flow field is the Stokes boundary layer, located close to the sphere surface (see e.g. Landau & Lifshitz 1978; Pozrikidis 1997). This region leads the development of the velocity profile, while the core of the flow field, halfway between the particles, exhibits a phase lag relative to the boundary layer. The dimension δ of the Stokes boundary layer is estimated from Re_ω as

$$\frac{\delta^*}{a^*} \sim \sqrt{\frac{4}{Re_\omega}}. \tag{3.1}$$

Figure 4(*c*) shows that as Re_ω decreases, the boundary layer extends further into the flow field, away from the sphere surface. At $Re_\omega = 25$ the dimensionless thickness of the Stokes boundary layer is 0.4. As can be seen in the figure, the peak in the developing velocity profile has extended further to the centre of the flow field than in

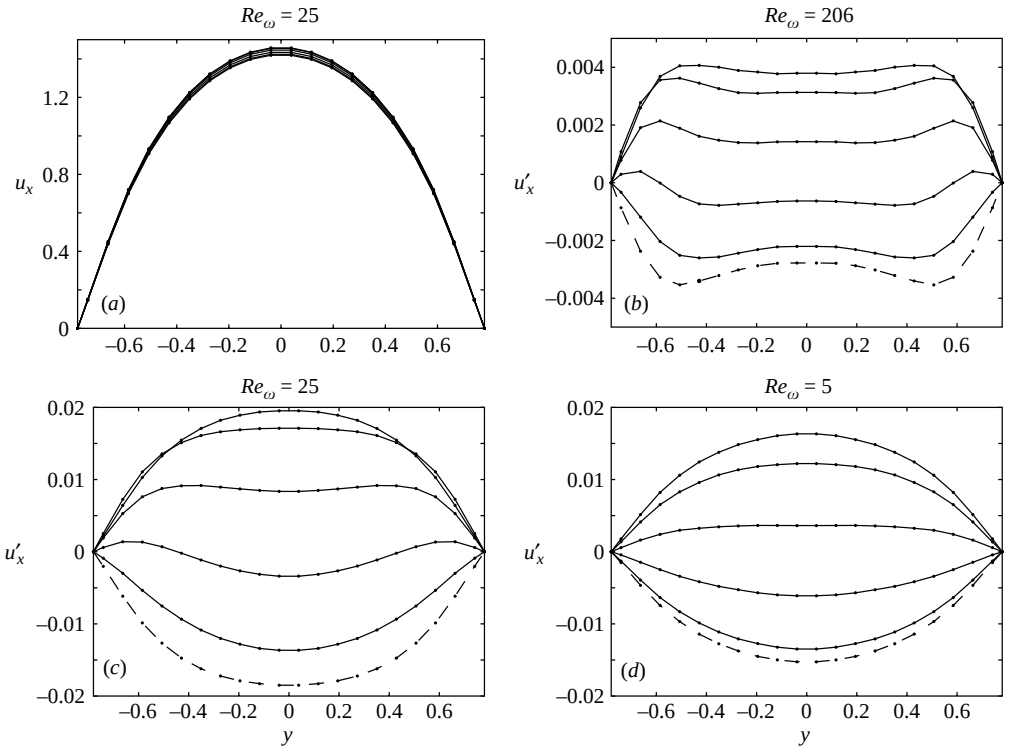

FIGURE 4. Dimensionless velocity profiles along the line connecting two spheres with $y = 0$ indicating the midpoint between the spheres. Re_ω values are indicated in the figures. (*a*) Streamwise velocity (u_x) profiles at six instants of time within half a cycle, (*b–d*) oscillatory part (u'_x) of the streamwise velocity profiles at these six times. Time proceeding in the upwards direction, starting at the dashed line ($Re_p = 1.3$, $a = 12.8$, $\phi = 0.1$).

figure 4(*b*). However, at maximum amplitude, the velocity profile no longer exhibits two maxima near the location of the boundary layer, but both boundary layers have merged in the centre of the flow field.

Figure 4(*d*) shows the velocity profile at even lower frequency. In this case δ is well in excess of half the separation distance between the spheres and the characteristic shape of the boundary layer in the velocity profile has practically disappeared throughout the whole oscillation cycle. The oscillation has become so slow that the flow field develops almost in pace with the fluctuating body force and a quasi-steady-state condition is reached.

These characteristic features are also visible in snapshots of the difference velocity fields $\boldsymbol{u}'$ in figure 5, which gives the difference flow fields at a single instance in time. At high Re_ω the Stokes boundary layer is clearly visible as a separate structure above and below the central sphere (figure 5(*a*)). The boundary layer extends outward and merges with its mirror image as Re_ω decreases.

The response of the unsteady velocity field is further characterized by the amplitude α_u and phase angle θ_u (see equation (2.4)). These are shown in figure 6 as a function of Re_ω, at three different volume fractions. In these figures the x-axis has been plotted on a log scale to show clearly the trends towards high and low Re_ω. Both the phase angle and the amplitude vary strongly with Re_ω; at low (high) Re_ω the phase angle goes towards zero (-0.5π) and the amplitude goes as $\alpha_u \to \alpha$ ($\alpha_u \to 0$).

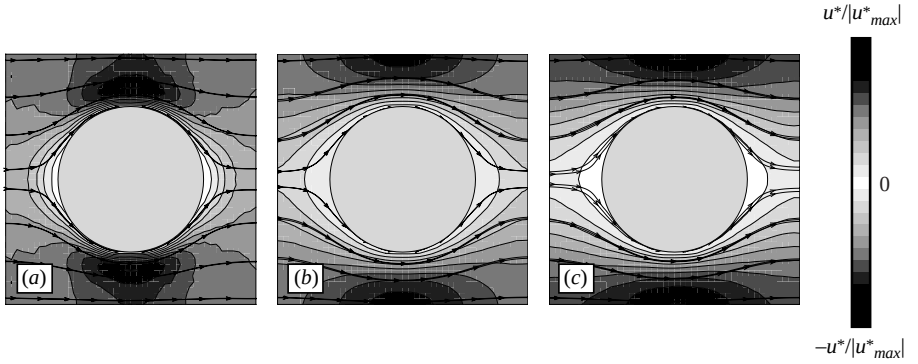

FIGURE 5. Snapshot of the fluctuating velocity field ($\boldsymbol{u}'$) at maximum negative amplitude (corresponding to the dashed line in figure 4(*b–d*)) $Re_\omega = 206$. (*a*) $Re_\omega = 25$, (*b*) and (*c*) $Re_\omega = 5$. The greyscale contours indicate the magnitude of the streamwise velocity component in each figure, the stream lines indicate the direction of the fluid velocity. Values are rescaled with the maximum velocity magnitude (u_{max}) in the flow field ($Re_p = 1.3$, $a = 12.8$, $\phi = 0.1$).

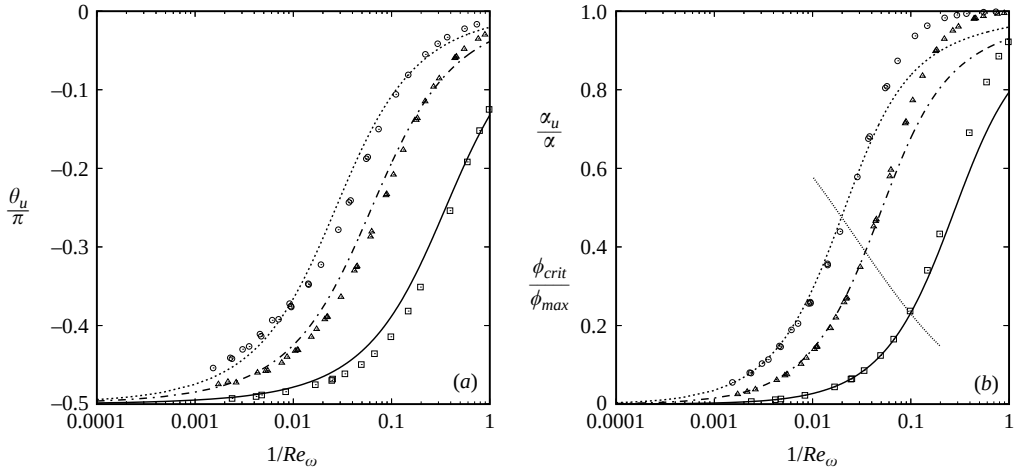

FIGURE 6. Response of (*a*) the phase angle (θ_u) and (*b*) amplitude ratio (α_u/α) in SCL geometry at $Re_p = 0.1$. $\phi = 0.10$ (□), $\phi = 0.27$ (△), and $\phi = 0.40$ (○). Lines give the response for unsteady Stokes flow at the corresponding volume fractions. The line in (*b*) crossing the response curves indicates Re_ω for $2\delta^* = d^*_{min}$ (3.3).

It is instructive to compare the simulated response of the unsteady flow with unsteady Stokes flow predictions. These predictions were computed by combining a ϕ-dependent drag force according to Sangani & Acrivos (1982) (see also § 2.4) with a virtual mass and history force according to equations (2.9) and (2.10) with regular values $f_v = 0.5$ and $f_h = 1.0$, indicating that as a first approximation, ϕ-corrections on the virtual mass and history force are ignored.

The general trends of the prediction correspond to those of the simulations. Figure 6(*a*) shows that the difference between simulated and predicted phase angle is at most 10%. The amplitude ratio in figure 6(*b*) shows a clearer deviation. For $Re_\omega \to \infty$, the amplitude ratio collapses with the values predicted by unsteady Stokes flow for all three volume fractions, but as the frequency is decreased the amplitude ratio rises to unity much more rapidly than predicted by the model.

The trends are in agreement with the image obtained from the velocity fields. At high Re_ω a small part of the fluid domain participates in the oscillating motion while the bulk of the flow field exhibits a strong phase lag (large negative phase angle) and a small amplitude. As the frequency decreases, the Stokes boundary layers expand and a larger part of the fluid participates in the oscillatory motion, resulting in a decrease of phase lag (less negative phase angle) and increase in amplitude.

Figure 6 shows the response upon a change in volume fraction. At constant Re_ω, both θ_u and α_u increase as ϕ increases. The influence of the periodic domain causes two effects. First, at higher ϕ a smaller volume of fluid is present to exhibit oscillatory motion, which contains less inertia and will be more responsive. Second, at increasing ϕ the separation between adjacent spheres allows less space for two separate Stokes boundary layers. As a result, the interaction of the boundary layers of adjacent spheres will occur at higher Re_ω, which is indicated by the dotted line in figure 6(*b*).

The effect of the geometry on the structure of the Stokes boundary layer can be estimated by equating the closest separation between two adjacent spheres to two times the boundary layer thickness, i.e. $2\delta^* = d^*_{min}$. At closer separation overlap of the Stokes boundary layers of adjacent spheres is expected. From the minimum separation between two spheres in an SCL array the corresponding critical volume fraction ϕ_{crit} for a given Re_ω is estimated as

$$\frac{d^*_{min}}{a^*} = \left(\frac{4\pi}{3\phi}\right)^{1/3} - 2, \tag{3.2}$$

while the relation between δ^* and Re_ω is given by (3.1). With some straightforward algebra, these equations can be rewritten to obtain a relation between ϕ and Re_ω,

$$\frac{\phi_{crit}}{\phi_{max}} = 8\left(4\sqrt{\frac{1}{Re_\omega}} + 2\right)^{-3}, \tag{3.3}$$

where ϕ_{max} indicates the volume fraction at which adjacent spheres touch.

In figure 6(*b*) the curve of (3.3) is indicated by the line that runs nearly perpendicular to the simulation data. Above this line we find $2\delta^* > d^*_{min}$ and the flow field is strongly influenced by the small separation. Below this line $2\delta^* < d^*_{min}$ holds and the influence of the geometry on the amplitude of the unsteady flow becomes small. One can see that this line roughly coincides with the onset of the departure between the simulation data and the unsteady Stokes flow prediction.

3.2. *Unsteady flow at* $Re_p = 25$

To explore the role of Re_p, a series of simulations have been carried out for a sphere in SCL geometry at $Re_p = 25$ and $\phi = 0.10$ and 0.27. At this Reynolds number the flow field contains a steady attached wake at the rear of the sphere.

In figures 7(*a*) and 7(*b*) the phase angle and amplitude are compared for $Re_p = 25$ and $Re_p = 0.1$. The largest difference is observed in the amplitude as $Re_\omega \to 0$. For $Re_p = 25$ this amplitude tends to be smaller than that of $Re_p = 0.1$. The amplitudes coincide as Re_ω becomes larger. At high Re_ω the unsteady fluid motion dominates the flow-field and the role of the background flow field becomes negligible. As a result, the amplitude of the fluid motion at different Re_p coincides as Re_ω becomes larger.

The unsteady part of the Navier-Stokes equations, (2.6), shows that the background flow-field contributes to the inertial terms $\bar{\boldsymbol{u}} \cdot \nabla \boldsymbol{u}' + \boldsymbol{u}' \cdot \nabla \bar{\boldsymbol{u}}$. These terms become important when the Strouhal number becomes small and the Reynolds number large, or equivalently, when $Re_\omega < Re_p$. In figure 8 flow-field snapshots are presented at $Re_p = 25$ to visualize this threshold. Re_ω is varied from $Re_\omega = 206$, figure 8(*a*, *d*), to

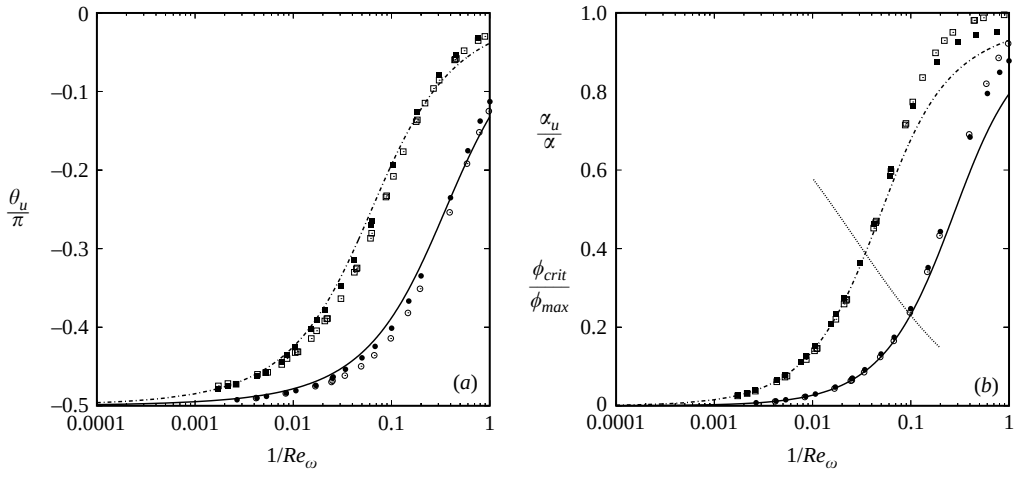

FIGURE 7. $Re_p = 25$ (filled symbols) compared with $Re_p = 0.1$ (open symbols) for (a) phase angle (θ_u) and (b) amplitude ratio (α_u/α). SCL geometry at $\phi = 0.1$ (●, ○) and $\phi = 0.27$ (■, □). Solid and dashed-dotted lines indicate the unsteady Stokes flow prediction, the line crossing the curves, in (b) indicates Re_ω for $2\delta^* = d^*_{min}$.

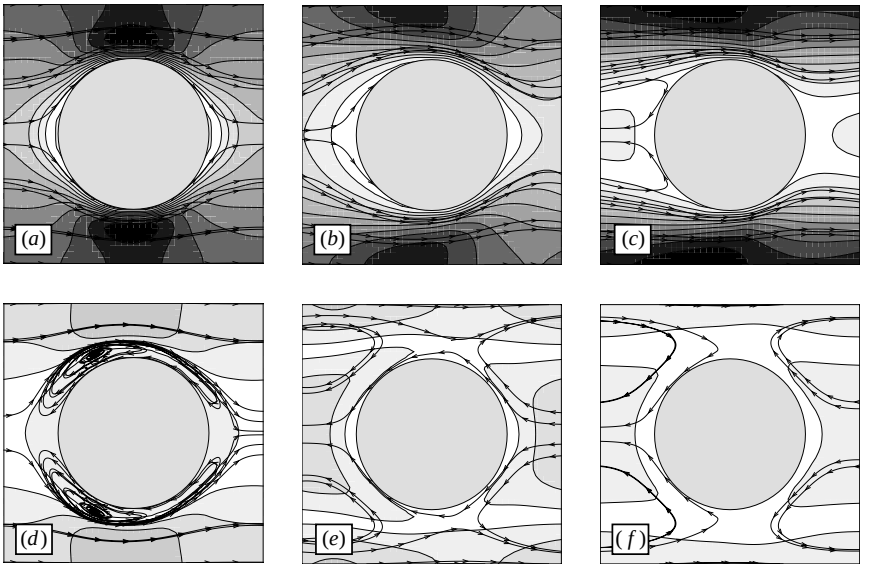

FIGURE 8. Snapshots of the $\boldsymbol{u}'$ flow field at $Re_p = 25$; flow field at maximum amplitude of u'_f and (a) $Re_\omega = 206$, (b) $Re_\omega = 26$ and (c) $Re_\omega = 5$; (d–f) flow field at $u'_f = 0$ and decreasing Re_ω. Mean flow from the right. Greyscale the same as in figure 5 ($a = 12.8, \phi = 0.1$).

$Re_\omega = 25$, figure 8(b, e), to $Re_\omega = 5$, figure 8(c, f). The snapshots were taken at two different moments in time; plots (a–c) were obtained at maximum amplitude of the mean fluctuating velocity, plots (d-f) just before the mean velocity changes sign.

In figure 8(a) the instantaneous flow field at maximum negative amplitude is given for the highest Re_ω. It is striking that the fluctuating flow field remains practically symmetric in the streamwise direction although the background flow field is highly asymmetric. The flow field in this figure is practically the same as that of figure 5(a)

at low Reynolds number, which demonstrates that at $Re_\omega \gg Re_p$ the contribution of the inertial terms is indeed negligible.

From figures 8(*a*) to 8(*b*) to 8(*c*), the impact of a decreasing Re_ω on the fluctuating velocity field is shown. In figures 8(*b*) and 8(*c*) a clear fore-aft asymmetry is present that is absent in figure 8(*a*) due to the dominant influence of the unsteady flow at high Re_ω.

Time proceeds from figures 8(*a*) to 8(*d*) at a single Re_ω. As the volume-averaged fluctuating velocity goes to 0, flow reversal sets in and closed streamlines appear. The closed streamlines appear because the outer zone of the flow field still moves in the direction of the flow at maximum amplitude, while the flow field close to the sphere has reversed. The downstream shift of the streamlines reveals the contribution of the background flow field.

At high Re_ω the vortex structure formed by the closed streamlines is attached closely to the sphere surface and exhibits a front side that reaches the upstream half of the sphere and a back side that stays closely attached to the sphere surface. Compared to figure 8(*d*), the vortex structures in figures 8(*e*) and 8(*f*), at lower Re_ω, have expanded considerably and the entire vortex structure has shifted downstream of the sphere. In these figures the front side of the vortex structure is shown in the left half of the image, downstream of the sphere, while the back side of the vortex reaches the front of its periodic neighbour, the right half of the image.

The small amplitude α is used to ensure that the response of the flow field remains in a linear regime, thus allowing the decomposition of the volume-averaged velocity as given in (2.4). In the case of higher Reynolds numbers it is not obvious that this decomposition still holds, since the wake structures become highly nonlinear. It was observed that in the phase of positive amplitude (not shown in the figures) the vortex structure in the difference velocity field is rotating in the same direction as the vortex in the background flow field, while in the phase of negative amplitude, given in the figures, the structures are rotating counter to the vortex of the background flow field. This reversal is a requirement as well as a guarantee that the assumption of a linear response is valid even at elevated Reynolds numbers.

4. The unsteady forces

4.1. *The total unsteady force*

In the earlier work of Mei *et al.* (1991) the amplitude of the unsteady force as a function of Re_ω was studied. In this section we demonstrate the analogy between our simulations and the work presented by these authors. Simulation results are discussed that demonstrate the impact of ϕ and Re_p on the behaviour of the total unsteady force acting on a sphere in an SCL geometry.

In Mei *et al.* (1991) the total unsteady force is given in complex form. In analogy to their approach the unsteady velocity and the unsteady force can be written as

$$u_f^* = u_{f,0}^*(1 + \alpha_u \exp\{-\mathrm{i}(\omega^* t^* + \theta_u - \pi/2)\}), \tag{4.1}$$

$$F_t^* = \bar{F}_t^* + F_{t,1}^* \alpha_u \exp\{-\mathrm{i}(\omega^* t^* + \theta_u - \pi/2)\} + O\left(\alpha_u^2\right), \tag{4.2}$$

with $F_{t,1}^*$ the first-order term of the unsteady force.

The unsteady force exhibits both an amplitude and phase angle that are different from the unsteady velocity. Therefore $F_{t,1}^*$ possesses both a real and an imaginary part. When normalized with the Stokes force F_{St}^*, the unsteady force can be written as

$$D(t) = F_t^*/F_{St}^* = D_S(Re_p, \phi) + (D_{1R} + \mathrm{i}D_{1I})\alpha_u \exp\{-\mathrm{i}(\omega^* t^* + \theta_u - \pi/2)\} \tag{4.3}$$

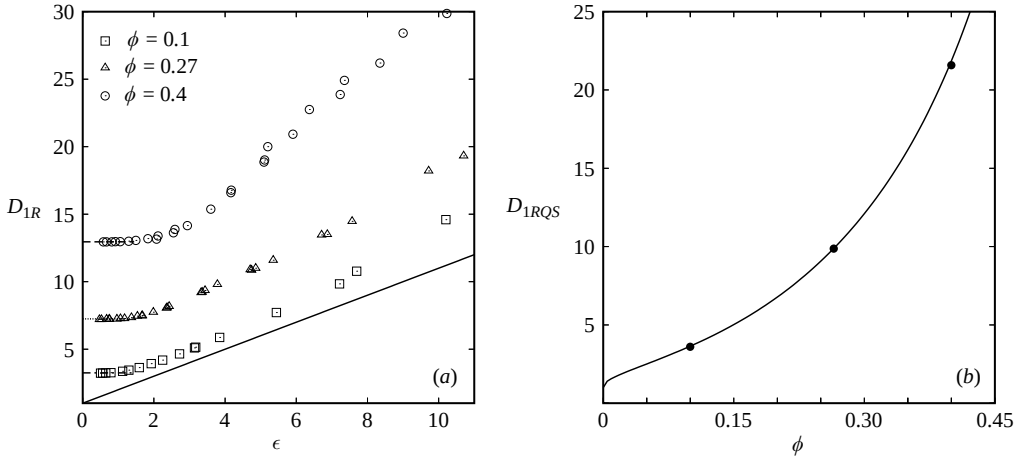

FIGURE 9. The real part of the unsteady force at three different volume fractions ϕ: (*a*) variation of D_{1R} with ϵ. The line indicates the real part of D_{1B} (equation (4.5)) which cuts the vertical axis at unity and yields a slope of unity; (*b*) variation of quasi-steady-state drag D_{1RQS} with ϕ. The line indicates $K(1-\phi)$ in the Stokes limit (Sangani & Acrivos (1982), see figure 2). ($Re_p = 0.25$).

where D_S is the steady drag force on the sphere (which varies with ϕ, Re_p and geometry) and D_{1R} and D_{1I} are the real and imaginary parts of the unsteady force amplitude.

It is illustrative to compare the total unsteady force to an analytical expression that can be derived from (2.9) and (2.10),

$$D_B(t) = K(1-\phi) + \left[K(1-\phi) + \tfrac{1}{2}\sqrt{Re_\omega} f_h(1-\mathrm{i}) - \tfrac{1}{9} Re_\omega f_v \mathrm{i}\right]\alpha_u \times \exp\{-\mathrm{i}(\omega^* t^* + \theta_u - \pi/2)\} \quad (4.4)$$

where the subscript B indicates the analytical solution. This equation is normalized using the Stokes drag force, as in equation (2.16), which also is used to define the drag coefficient K. The square brackets indicate the unsteady part of the force. The term $K(1-\phi)$ indicates the steady and quasi-steady-state contributions to the drag force, while the second term in the unsteady part corresponds to the Basset history force and the last term to the virtual mass force. In this relation the coefficients K, f_h and f_v are usually modified to account for effects of volume fraction, Reynolds number and geometry. In the case of an isolated oscillating sphere in an infinite medium at unsteady Stokes flow conditions (i.e. $\phi \to 0$, $K \to 1$, $f_h \to 1$, $f_v \to 1/2$), the unsteady part of this expression reduces to the familiar analytic form given by Landau & Lifshitz (1978),

$$D_{1B} = 1 + (1-\mathrm{i})\epsilon - \mathrm{i}\tfrac{2}{9}\epsilon^2 \quad (4.5)$$

where $\epsilon = \sqrt{Re_\omega/4}$ is the parameter used by Mei *et al.* (1991) to characterize unsteady flow conditions. A comparison between (4.3) and (4.4) shows that D_{1R} relates to the sum of the quasi-steady-state drag force and the real part of the Basset force and is expected to vary proportionally to $\sqrt{Re_\omega}$, while D_{1I} relates to the sum of the Basset and virtual mass force and varies with both $\sqrt{Re_\omega}$ and Re_ω.

In figure 9 the behaviour of the unsteady force on a particle at $Re_p = 0.25$ at three different volume fractions and over a wide range of ϵ is given. Figure 9(*a*) shows

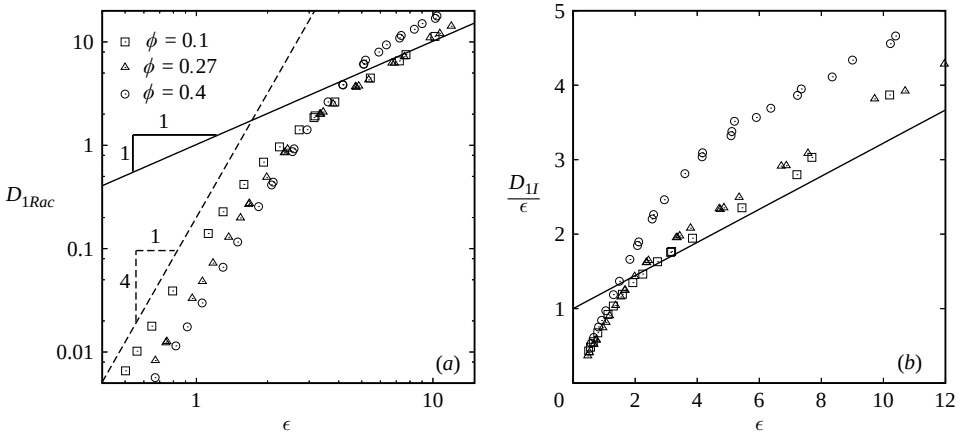

FIGURE 10. (*a*) Variation of the acceleration term D_{1Rac} with ϵ. The solid line indicates the unsteady Stokes solution $D_{1Bac} = \epsilon$. The dashed line with a slope of 4 is drawn to guide the eye. (*b*) Variation of the imaginary term D_{1I}/ϵ with ϵ. The line corresponds to (4.5) with $f_v = 0.5$ and $f_h = 1.0$ ($Re_p = 0.25$).

that D_{1R} contains a low- and a high-ϵ regime. For $\epsilon \to 0$ D_{1R} approaches a constant value, the quasi-steady-state drag force, that increases with ϕ. Towards high ϵ, D_{1R} increases linearly with ϵ, as anticipated from (4.4) and (4.5). The figure shows that for intermediate $\phi = 0.1$ and $\phi = 0.27$ the slope tends to be somewhat larger than unity, while for $\phi = 0.4$ the slope of the high-ϵ end of the curve is clearly increased.

The quasi-steady-state forces D_{1RQS} are indicated in figure 9(*a*) by the short horizontal lines that extend the data points to zero. Towards smaller Re_ω the oscillation time scale increases. Simulations were performed for at least three entire oscillation cycles. Therefore, at low Re_ω the duration of the simulations increases considerably. As a result, the smallest Re_ω values that were practically obtainable with our simulations were around $Re_\omega \simeq 1$. The limiting value of D_{1R} as $\epsilon \to 0$ was estimated from the simulations at these lowest Re_ω values.

In figure 9(*b*) D_{1RQS} is plotted against ϕ together with a line that indicates $K(1-\phi)$, the steady drag on a sphere in Stokes flow in an SCL arrangement (Sangani & Acrivos 1982). The figure shows that at this low Reynolds number the quasi-steady-state force coincides with the steady-state values. Therefore nonlinear contributions to the force that appear at higher Reynolds number are negligible at $Re_p = 0.25$.

Subtracting the quasi-steady-state force from the real part of the unsteady force gives the acceleration-dependent component of the unsteady force, $D_{1Rac} = D_{1R} - D_{1RQS}$. This term is plotted in figure 10(*a*). The figure shows that as $\epsilon \to 0$ D_{1Rac} decays rapidly as ϵ^4, similarly to what was observed by Mei *et al.* (1991). This rapid decay was interpreted by Mei *et al.* (1991) as an interplay between the unsteady flow field and the steady background flow field. In the unsteady flow field vorticity is transported away from the sphere surface by diffusion and decays up to the Stokes boundary layer thickness δ^*. In a steady flow field at higher Reynolds number, convective transport of vorticity occurs inside the Oseen region with a dimension of a^*/Re_p. For an isolated sphere in a regime where the Stokes boundary layer exceeds the dimensions of the Oseen region, the vorticity, generated at the surface of the sphere, is transported by convection in the Oseen region before the vorticity has extended to the Stokes region.

Mei *et al.* (1991) show that for an isolated sphere at $Re_p = 0.2$ and $\epsilon = 1$, D_{1Rac} is practically indistinguishable from the unsteady Stokes solution ($\epsilon = 1$ is chosen for easy comparison). Figure 10(a) shows, in contrast, that for a sphere in an SCL arrangement at $\epsilon = 1$ and $\phi \geqslant 0.1$, $D_{1Rac} < D_{1Bac}$ and the steep decay of D_{1Rac} as ϵ^4 is clearly present. At $\epsilon = 1$, the critical volume fraction above which the boundary layers are interacting is $\phi_{crit} = 0.065$. The simulations presented in figure 10(a) all exceed ϕ_{crit} at $\epsilon = 1$ and boundary layer interaction takes place for all three volume fractions. For decreasing volume fractions the decay starts at a lower ϵ. Apparently, the limitations the geometry poses to the expanding dimensions of the Stokes boundary layer enhances the transport of vorticity in a manner similar to that achieved by convection in the Oseen region for isolated spheres.

In contrast with the results on isolated spheres (Mei *et al.* 1991), towards higher ϵ D_{1Rac} exceeds the Stokes solution $D_{1Bac} = \epsilon$, given by the solid line. At the high-ϵ end of the curve, figure 9(a) showed that the slope of D_{1R} increases with ϕ. Therefore with increasing ϵ the D_{1Rac} curve at $\phi = 0.4$ crosses D_{1Bac} at lower ϵ and obtains a larger value in the high-ϵ range than the curves at lower ϕ.

In figure 10(b) the imaginary part of the unsteady force is plotted as D_{1I}/ϵ. This form was chosen since a linear relation between D_{1I}/ϵ and ϵ is anticipated, given that from (4.4),

$$\frac{D_{1I}}{\epsilon} = f_h + \frac{4}{9} f_v \epsilon \tag{4.6}$$

can be obtained. This relation is plotted by the line for $f_v = 0.5$ and $f_h = 1.0$.

Figure 10(b) shows that D_{1I}/ϵ depends both on ϕ and on ϵ and exhibits a low- and a high-ϵ regime that deviates from the unsteady Stokes solution (4.6). Towards low ϵ, instead of obtaining a constant value, D_{1I}/ϵ drops off linearly to zero at all three ϕ values. This implies that in the quasi-steady-state regime the contributions of the history and virtual mass force reduce to zero in the imaginary part of the unsteady force. This is comparable to the result of Mei *et al.* (1991), who show that for an isolated sphere in the limit $\epsilon \to 0$ the history contribution to D_{1I} varies as ϵ^2.

Towards large ϵ a clear effect of the volume fraction is present. D_{1I}/ϵ at high ϵ runs parallel to the unsteady Stokes limit line, indicating a practically constant virtual mass coefficient. The increasing offset at higher ϕ suggests an increasing contribution of the Basset history force at larger ϵ. This is in agreement with the increasing slope observed in the high-ϵ range of the D_{1R} curve of figure 9(a).

To study the impact of the Reynolds number, simulations at constant volume fraction of $\phi = 0.27$ have been performed in the range $Re_p = 0.25$–60.0. D_{1R} is given in figure 11(a). Again, at the low-ϵ end D_{1R} tends to level off to a quasi-steady-state value for all Reynolds numbers. At larger values of ϵ and low Re_p, D_{1R} increases linearly with ϵ. At higher Reynolds numbers D_{1RQS} attains higher values, causing an increase in offset at $\epsilon \to 0$. Yet, in the higher ϵ range D_{1R} shifts towards the data points of the low-Reynolds-number case. With increasing Reynolds number this shift becomes more pronounced and the low-Reynolds-number curve is approached only at higher ϵ values. At higher Reynolds number, the nonlinear terms of the Navier–Stokes equations make an increasing contribution that is overwhelmed by the unsteady flow only at the highest ϵ ranges.

The variation of the quasi-steady-state drag D_{1RQS} with the Reynolds number is shown in figure 11(b) as circles. For comparison the true steady-state drag force D_S, obtained from steady-state simulations, is also plotted in this figure. The drag curve exhibits the typical $O(Re^2)$ increase in the low-Reynolds-number range that shifts to

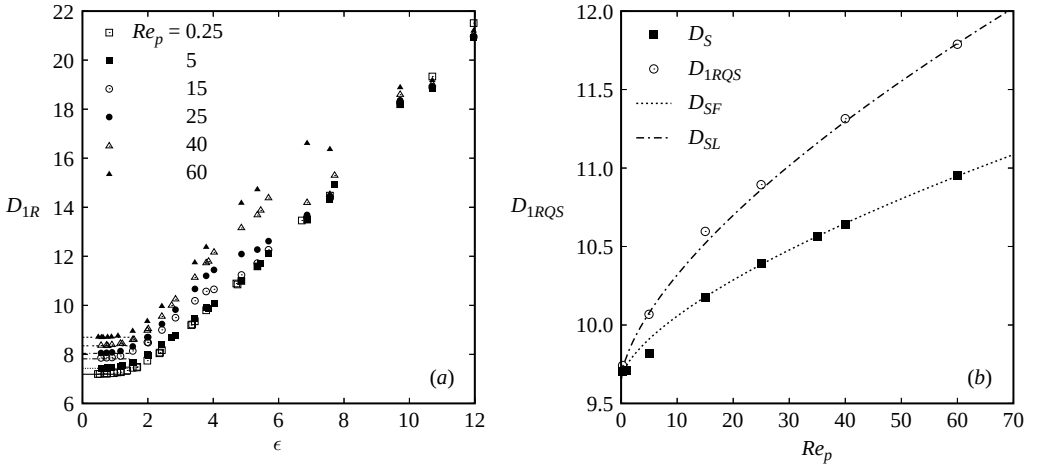

FIGURE 11. (*a*) Variation of D_{1R} with ϵ at $\phi = 0.27$ over a range of Re_p. (*b*) Comparion of D_{1RQS} with D_S as a function of Re_p. The dotted line gives D_{SF}, the dashed-dotted line gives the linearized prediction D_{SL} (equations (4.7) and (4.8)).

a much slower steady rise at higher Reynolds numbers (see Hill *et al.* 2001*b*). The high-Reynolds-number part ($Re_p > 10$) of the steady-state curve given in figure 11(*b*) has been fitted with an empirical equation of form similar to the drag curve for an isolated sphere as used by Mei *et al.* (1991):

$$D_{SF} = p_1 + p_2 Re_p^{p_3} \tag{4.7}$$

(fit result; $p_1 = 9.655 \pm 0.080$, $p_2 = 0.089 \pm 0.027$, $p_3 = 0.653 \pm 0.061$). As shown by Mei *et al.* (1991), the quasi-steady-state drag force can be estimated from this relation as

$$D_{SL} = p_1 + p_2(1 + p_3) Re_p^{p_3}. \tag{4.8}$$

This prediction is also presented in figure 11(*b*). The figure shows that D_{SL} accurately captures the quasi-steady-state drag force.

4.2. *Characteristics of the unsteady pressure and friction forces*

To obtain more insight into the nature of the unsteady forces, they were also separated into pressure and friction force components. In analogy to the representation of the volume-averaged fluid velocity, the forces can also be represented as

$$F_i^* = \bar{F}_i^* + F_i'^* = F_{i,0}^*[1 + \alpha_i \sin(t + \theta_i)]. \tag{4.9}$$

In this representation the key parameters that describe the unsteady forces are the response amplitude α_i and phase angle θ_i (i indicates pressure (p), friction (f) or total (t) force component). The subscript 0 indicates the steady-state forces

$$F_{t,0}^* = \beta^* u_{f,0}^*; \quad F_{p,0}^* = R_p \beta^* u_{f,0}^*; \quad F_{f,0}^* = (1 - R_p)\beta^* u_{f,0}^*. \tag{4.10}$$

In figure 12*a* typical time cycle of the body force that drives the flow, the fluid velocity, and the oscillating forces are given. The figure shows that the unsteady forces lag the body force g, but have a phase lead relative to the fluid velocity, while the friction component F_f' has a smaller phase lead than the pressure component F_p'. This typical behaviour was also observed by Chang & Maxey (1994) for unsteady forces acting on an isolated sphere.

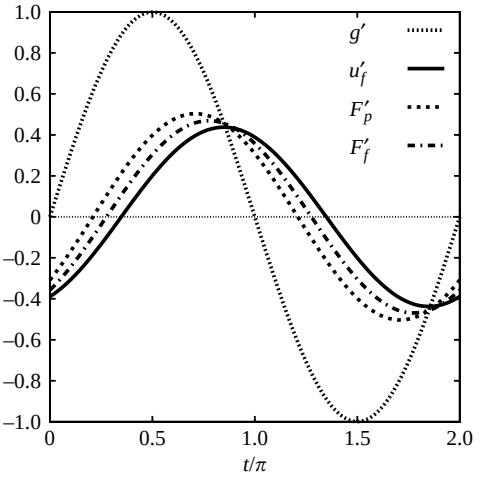

FIGURE 12. Time cycle of the oscillating part of the body force g', the fluid velocity u'_f and the pressure and friction forces F'_p and F'_f, normalized with the forcing amplitude α ($Re_p = 0.25$, $Re_\omega = 5.0$, $a = 12.8$, $\phi = 0.10$).

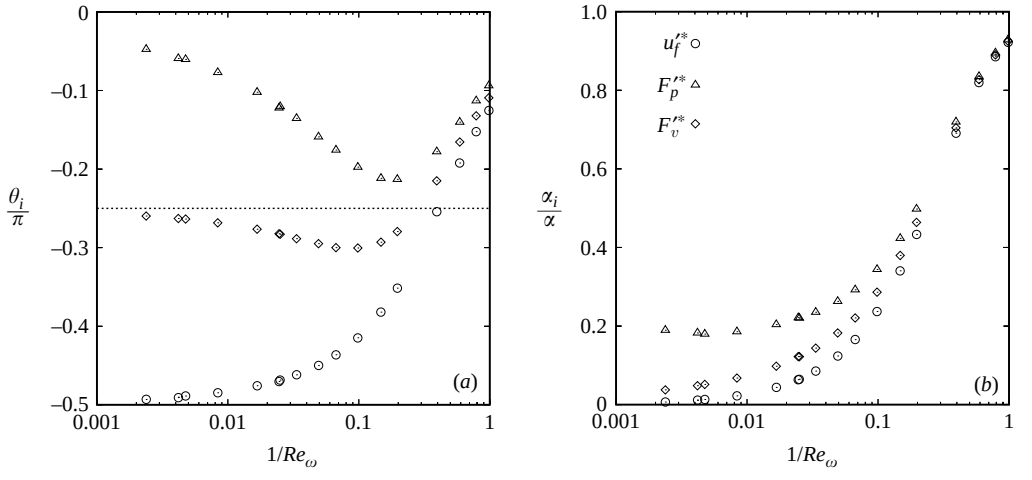

FIGURE 13. Phase angle (a) and amplitude (b) of the fluid velocity, pressure force F'_p and friction force F'_f ($Re_p = 0.25$, $\phi = 0.10$).

Figure 13(a) summarizes the variation of phase angle of the unsteady forces and the fluid velocity with Re_ω. It is clear that the order of the phase angles of the pressure and friction forces and the fluid velocity remain unchanged over the entire range of Re_ω. It is also clear that the phase angle of the unsteady forces approaches that of u'_f at low Re_ω values. This is entirely reasonable as at low Re_ω values the unsteady flow field approaches a quasi-steady-state structure. As Re_ω increases, θ_u goes monotonically to -0.5π, while θ_p and θ_f exhibit a minimum. As $Re_\omega \to \infty$, we observe that $\theta_p \to 0$ and $\theta_f \to -0.25\pi$.

Figure 13(b) shows the dependence of the amplitudes on Re_ω. For low Re_ω, the relative amplitudes are nearly equal. For high Re_ω, α_u and α_f almost reduce to 0 while α_p reaches a constant value. In this regime the flow field oscillates so vigorously

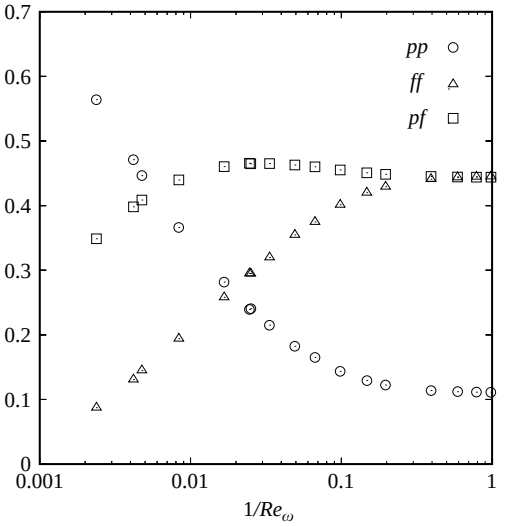

FIGURE 14. Relative contribution of the pressure and friction forces to the total unsteady forces as a function of $1/Re_\omega$ ($Re_p = 0.25, \phi = 0.10$). pp indicates the contribution of the pressure force, ff indicates the contribution of the fricton force and pf indicates the cross-correlation of pressure and friction force (see (4.12)).

that velocity gradients at the surface hardly develop and the pressure force becomes the dominant contribution to the overall force. The relative amplitude α_p/α becomes independent of Re_ω since the pressure field develops practically instantaneously.

By setting $F_t^* = F_p^* + F_f^*$ and only looking at the unsteady part of the forces we get a non-dimensional equation for the fluctuating part of the total unsteady force,

$$\alpha_t \sin(t + \theta_t) = R_p \alpha_p \sin(t + \theta_p) + (1 - R_p)\alpha_f \sin(t + \theta_f) \tag{4.11}$$

with $R_p = F_{p,0}/F_{t,0}$. From this equation we obtain an expression for the composition of the amplitude α_t from the pressure and friction force components,

$$\alpha_t^2 = (\alpha_p R_p)^2 + (\alpha_f(1 - R_p))^2 + 2(\alpha_p \alpha_f R_p(1 - R_p)) \cos(\theta_p - \theta_f), \tag{4.12}$$

which can be used to demonstrate how, with a variation of Re_ω, each component contributes to the total force.

In figure 14, the contributions of the three terms on the right-hand side of this equation are plotted, where pp indicates the pressure force term, ff indicates the friction force term and pf is used to indicate the cross-correlation between pressure and friction forces. The data are normalized with α_t^2, such that the sum of the terms becomes unity.

At low Re_ω, $(\theta_p - \theta_f) \to 0$, $\alpha_p \to \alpha_f$, and therefore the relative contributions of the three terms on the right-hand side of (4.12) are simply determined by R_p, which does not vary with Re_ω.

Towards high Re_ω, figure 14 shows that the distribution of the total force over the pressure and friction components changes drastically. The pp contribution increases strongly as Re_ω increases, while the ff contribution decreases. The term pf remains positive as Re_ω increases and the forces therefore do not counteract each other. Since ff tends to zero as $Re_\omega \to \infty$, their cross-correlation also decays to zero in this range. This demonstrates, as anticipated, that at high Re_ω the main contribution to the total force on the sphere comes from the pressure force.

4.3. *The analogy between the pressure and friction forces and the virtual mass and history forces*

As figure 13(*a*) has shown that, towards high Re_ω, the pressure force becomes in phase with the driving body force, while the friction force tends to a phase angle of $-(1/4)\pi$. In the limit $Re_\omega \to \infty$, the phase angles suggest that the virtual mass is attributed to the pressure force and the history force to the friction force. This is in correspondence with the origin of the history force, which is a purely viscous force (Crowe *et al.* 1997), and the observation by a number of authors (Chang & Maxey 1994, 1995; Rivero *et al.* 1991) that the virtual mass force can be attributed to the pressure force. Rewriting the pressure and friction forces thus gives

$$\begin{aligned} F_p^* &= F_{p,0}^* + F_p'^* + F_v^* \\ &= R_p\beta_0^* u_{f,0}^* + R_p\beta_p^* u_f'^* + \rho_f^*\phi(1-\phi)f_v\frac{\partial u_f^*}{\partial t^*} \end{aligned} \tag{4.13}$$

and

$$\begin{aligned} F_f^* = F_{f,0}^* + F_f'^* + F_h^* &= (1-R_p)\beta_0^* u_{f,0}^* + (1-R_p)\beta_f^* u_f'^* \\ &\quad + \frac{9}{2a^*}\sqrt{\frac{\rho_f^*\mu^*}{\pi}}\phi(1-\phi)f_h\int_{-\infty}^{t^*}\frac{\partial u_f^*}{\partial t^*}\frac{1}{\sqrt{t^*-\tau^*}}\,\mathrm{d}\tau^* \end{aligned} \tag{4.14}$$

where the unsteady drag coefficient has been separated into pressure and friction parts, β_p^* and β_f^* and are allowed to vary with Re_ω.

We can rewrite the unsteady part of the forces in dimensionless form as

$$\frac{F_p'^*}{F_{p,0}'^*} = \frac{\alpha_p}{\alpha_u}\sin(t+\theta_p) \tag{4.15}$$

$$= \frac{\beta_p^*}{\beta_0^*}\sin(t+\theta_u) + \frac{f_v Re_\omega}{9R_p(1-\phi)K}\cos(t+\theta_u) \tag{4.16}$$

$$= V_p\sin(t+\theta_u) + A_p\cos(t+\theta_u) \tag{4.17}$$

and

$$\frac{F_f'^*}{F_{f,0}'^*} = \frac{\alpha_f}{\alpha_u}\sin(t+\theta_f) \tag{4.18}$$

$$= \frac{\beta_f^*}{\beta_0^*}\sin(t+\theta_u) + \frac{f_h\sqrt{Re_\omega}}{2(1-R_p)(1-\phi)K}(\sin(t+\theta_u)+\cos(t+\theta_u)) \tag{4.19}$$

$$= V_f\sin(t+\theta_u) + A_f(\sin(t+\theta_u)+\cos(t+\theta_u)) \tag{4.20}$$

where the forces are normalized by $F_{p,0}'^* = \beta_0^* R_p u_{f,0}^* \alpha_u$ and $F_{f,0}'^* = \beta_0^*(1-R_p)u_{f,0}^*\alpha_u$. The variables V_i and A_i ($i = p, f$) are introduced for the terms associated with the fluid velocity (the drag force) and acceleration (the apparent virtual mass and history forces), respectively. The velocity and acceleration terms are obtained by evaluating (4.15) and (4.18) at the phase angle where V_i or A_i becomes zero. For example, we obtain A_p at $t = -\theta_u$ and V_p at $t = -\theta_u + 0.5\pi$.

The above decomposition is made based on the limiting case of $Re_\omega \to \infty$, in which case the flow field tends to inviscid flow. In the literature the convention is that the virtual or added mass force is considered strictly an inviscid force. As Re_ω decreases, the pressure force will pick up contributions that stem from viscous flow and that cannot be separated from purely inviscid terms. Therefore, the changes in the

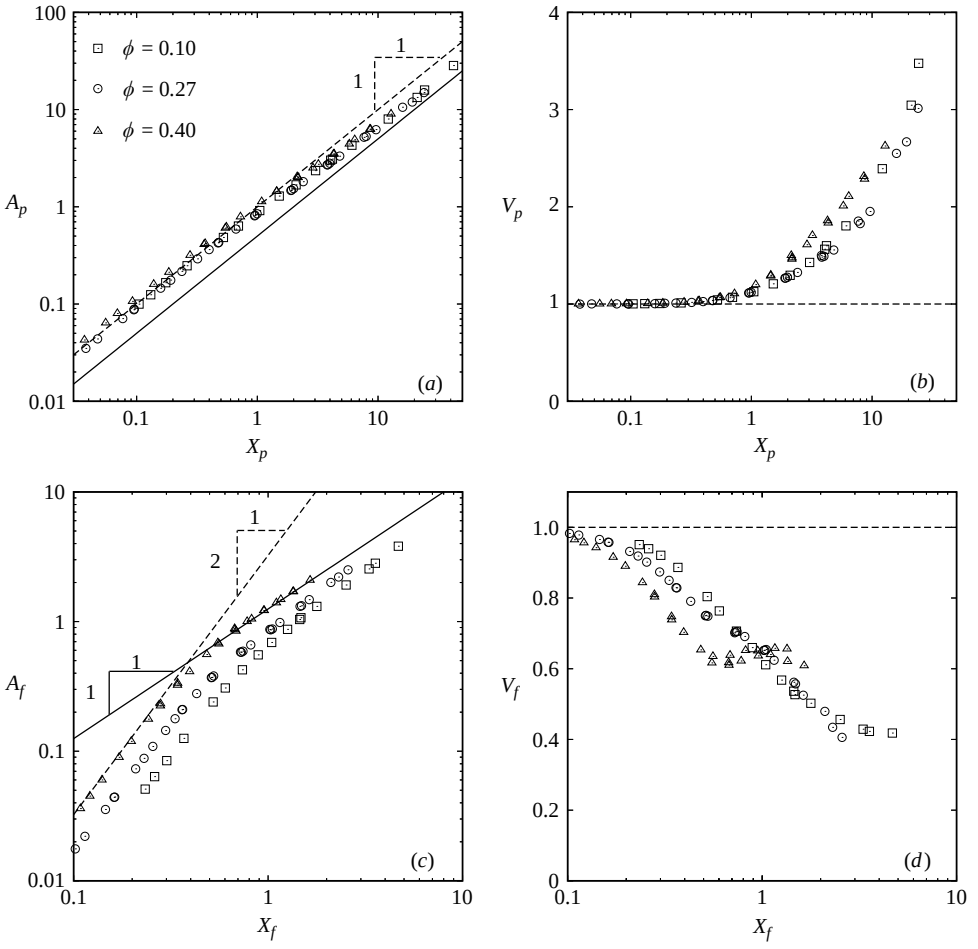

FIGURE 15. The acceleration and velocity terms of the unsteady pressure and friction forces at three different volume fractions for $Re_p = 0.25$; (*a*) and (*b*) acceleration and velocity terms of the pressure force, (*c*) and (*d*) acceleration and velocity terms of the friction force. The lines indicate the limits towards high (solid line) and low (dashed line) X_p and X_f. In (*a*) lines indicate $1.0X_p$ (dashed) and $0.5X_p$ (solid).

accelarative part of the pressure force as a function of Re_ω will further be discussed using the term 'apparent' virtual mass force.

There is a direct analogy between the above equations (4.15)–(4.20) and D_{1R} and D_{1I}. The real part D_{1R} corresponds to the sum of all the sine terms, while D_{1I} corresponds to the sum of all the cosine terms:

$$D_{1R} = K(1-\phi)(R_p V_p + (1-R_p)(V_f + A_f)) \tag{4.21}$$

and

$$D_{1I} = K(1-\phi)(R_p A_p + (1-R_p)A_f). \tag{4.22}$$

In figure 15 the pressure and friction forces of simulations performed at $Re_p = 0.25$ and three different values of ϕ are evaluated using equations (4.15)–(4.20). Equation (4.16) suggests that a proper scaling that corrects for the variation in ϕ is obtained

when the pressure force is plotted against $X_p = Re_\omega/9R_p(1-\phi)K$, while (4.19) suggests $X_f = \sqrt{Re_\omega}/2(1-R_p)(1-\phi)K$ may provide a good scaling for the friction force.

Figure 15(*a*) shows that by scaling the x-axis with X_p, the data of the acceleration term A_p at different ϕ values collapse to one curve. The velocity term in figure 15(*b*) shows a modestly good collapse. In contrast to the pressure force, figures 15(*c*) and 15(*d*) show that the friction force amplitude and phase angle at different volume fractions do not collapse onto a single master curve. The acceleration term A_f remains dependent on ϕ, with data at higher ϕ shifting to lower values of X_f.

In figures 15(*a*) and 15(*c*), lines have been drawn to indicate the slope at which the simulation data approach the high (solid line) or low (dashed line) X_p and X_f limits. At high X_p (figure 15*a*), A_p approaches $0.5X_p$, which is equivalent to $f_v \to 0.5$. As $X_p \to 0$, $A_p \to 1.0X_p$, corresponding to $f_v \to 1.0$. The transition from the low- to high-X_p regime takes place around $X_p \sim 1$.

Our simulations reveal that the unsteady drag coefficient $\beta_p^*(=V_p\beta_0^*)$ is not a constant, but varies with X_p. At low X_p values, $V_p \to 1.0$; however, at high X_p values, it increases strongly (figure 15*b*).

At high X_f the acceleration term A_f (figure 15*c*) is proportional to X_f (or, equivalently, to $\sqrt{Re_\omega}$), in correspondence with the regular history force term. For $X_f \to 0$, the A_f term decays to zero as X_f^2 as shown in figure 15(*c*).

The variation of the friction force with ϕ agrees well with the observations on the flow field in the SCL geometry. As was discussed in § 3.1, the condition $2\delta^* = d_{min}^*$ gives a relation between ϕ and a critical Re_ω, below which interaction between the boundary layers of neighbouring particles occurs. The critical X_f values calculated in this manner (0.48, 0.30 and 0.23, corresponding to ϕ values of 0.1, 0.27 and 0.4) are consistent with the location of the transition point between the low- and high-X_f ranges in figure 15(*c*).

Figure 15(*d*) shows that V_f tends to a value of 1.0 at low X_f while towards high X_f the velocity term decays exponentially. The figure also shows that there is a clear effect of volume fraction on V_f. At low X_f, the data at the highest ϕ decay the steepest. Around $X_f \sim 1$ the values of V_f with $\phi = 0.4$ level off and only at the highest X_f seem to decrease again. Thus the drag coefficient β_f^* varies appreciably with both Re_ω and ϕ.

The effect of the Reynolds number on the pressure and friction forces is plotted in figure 16(*a–d*). The general trend is that the acceleration terms exhibit a negligble change due to the change in Reynolds number. The scaling of X_p and X_f contains a correction for the Reynolds number in the term $R_p(1-\phi)K$ and both A_p and A_f data at different Reynolds numbers collapse to the same curve.

The velocity terms are clearly sensitive to the change in Reynolds number. The term V_p in the limit $X_p \to 0$ goes to a value of 1 at $Re_p = 0.25$, but with increasing Reynolds number the limiting value also increases. V_f in the limit $X_f \to 0$ decreases with increasing Reynolds number. As the quasi-steady-state drag force (see figure 11*b*) is larger than the steady-state drag force, the increase of V_p is larger than the decrease in V_f.

A comparison between figure 11(*a*) and figure 16 further reveals that the increment of D_{1R} in intermediate ranges of ϵ is entirely the result of the change in V_p and V_f with increasing Reynolds number. While A_p hardly changes with Re_p, V_p increases with X_p and exhibits a clear increment towards higher values of Re_p, while towards the highest X_p the curves tend to collapse again. Similarly, A_f remains unchanged with increasing Re_p, while V_f decreases with X_f and exhibits an increasingly strong sigmoidal shape around $X_f = 1$ as Re_p increases.

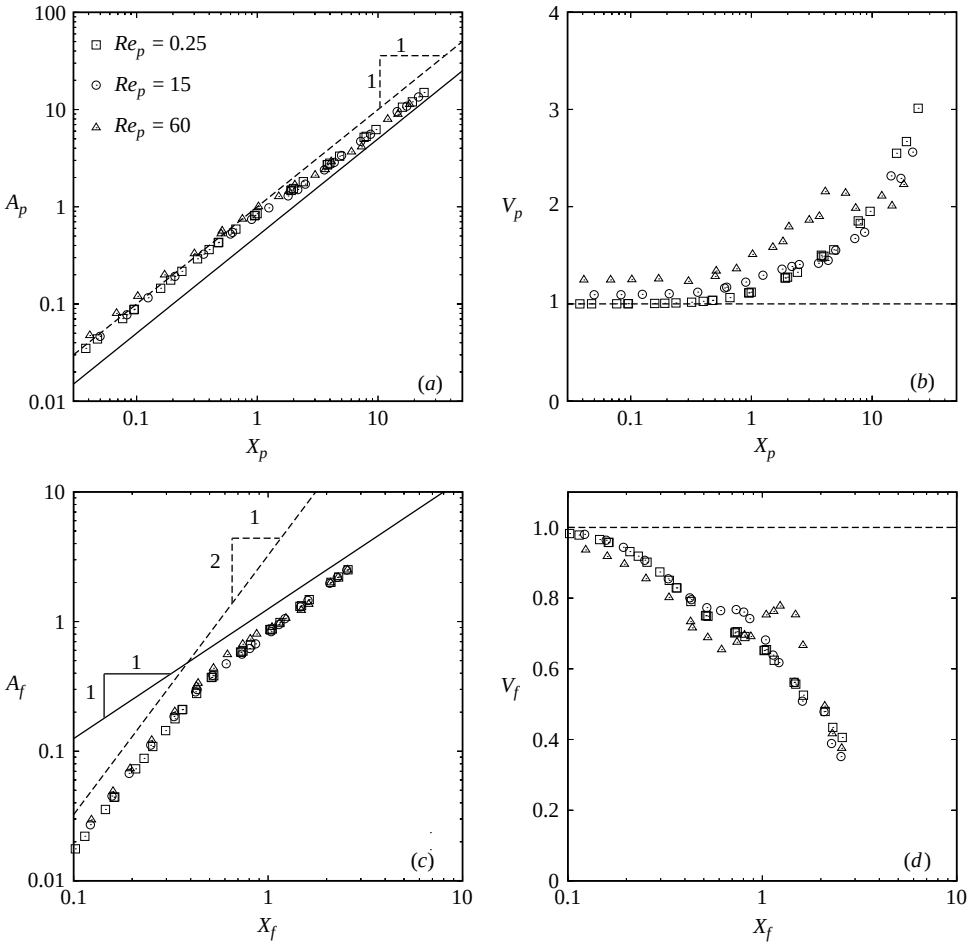

FIGURE 16. The acceleration and velocity terms of the unsteady pressure and friction forces at three different Reynolds numbers at $\phi = 0.27$; (*a*) and (*b*) acceleration and velocity terms of the pressure force, (*c*) and (*d*) acceleration and velocity terms of the friction force. The lines indicate the limits towards high (solid line) and low (dashed line) X_p and X_f. In (*a*) lines indicate $1.0X_p$ (dashed) and $0.5X_p$ (solid).

Chang & Maxey (1994) noted that steady oscillatory flow is a very specific case of unsteady flow, and questioned whether oscillatory flow is appropriate to develop models for the history kernel. Kim *et al.* (1998) demonstrated that the history kernel originally devised by Mei & Adrian (1992) is inaccurate in predictions of random unsteady motion on an isolated sphere. Given these, we have limited our efforts to simply examining the behaviour of the history force and did not attempt to develop new models or kernels.

4.4. *The velocity and acceleration contributions to the total force* $F_t'^*$

Our discussion thus far has focused on decomposing the total unsteady force into pressure and friction force components. We now examine the composition of the same total unsteady force in terms of the velocity and acceleration terms. The three groups that contribute to the total unsteady force are the unsteady drag force, given by the velocity term V, and the acceleration terms $R_p A_p$ and $(1 - R_p)A_f$, which are related

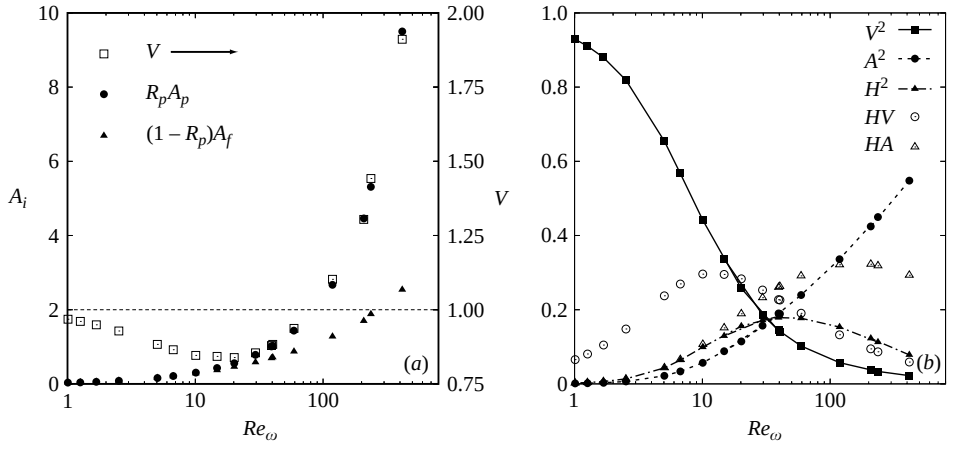

FIGURE 17. Total unsteady force at $Re_p = 0.25$ and $\phi = 0.1$; (*a*) the normalized drag coefficient β'^*/β_0^* (scale on right-hand side axis, dashed horizontal line indicates $V = 1.0$), the pressure and friction force acceleration terms (i.e. apparent virtual mass and the history forces) amplitude, (*b*) the normalized contribution of the drag, apparent virtual mass and history forces to the overall force amplitude.

to the apparent virtual mass and history force respectively. The total unsteady force can be written as

$$\begin{aligned} F_t'^* &= F_d'^* + F_v^* + F_h^* \\ &= F_0^* V \sin(\omega^* t^* + \theta_u) + F_0^* R_p A_p \cos(\omega^* t^* + \theta_u) \\ &\quad + F_0^*(1 - R_p) A_f (\sin(\omega^* t^* + \theta_u) + \cos(\omega^* t^* + \theta_u)) \end{aligned} \tag{4.23}$$

where $F_0^* = \beta_0^* u_{f,0}^*$, and $V = \beta'^*/\beta_0^*$ with β'^* the unsteady drag coefficient ($\beta'^* = R_p\beta_p^* + (1 - R_p)\beta_f^*$).

For the case $Re_p = 0.25$ and $\phi = 0.1$, the Re_ω dependence of these groups is given in figure 17(*a*). In the quasi steady state, when $Re_\omega \to 0$, the figure shows $V \to 1$, $A_p \to 0$ and $A_f \to 0$. As was shown earlier, at low Reynolds number the quasi-steady-state drag coefficient tends to its true steady-state value while the apparent virtual mass and history forces become negligible. As Re_ω increases, V passes through a minimum, about 20% below its steady-state value, and then increases monotonically. Around $Re_\omega \sim 100$ we find $V > 1$. The A_p and A_f terms increase monotonically with Re_ω and become much larger than V.

Even though at increasing Re_ω the A_p and A_f terms in figure 17(*a*) become much larger than V, it does not necessarily mean that their contribution to the total unsteady force is the largest. The composition of $F_t'^*$ was evaluated earlier in figure 14 via the decomposition of α_t into α_p and α_f contributions (see also (4.11) and (4.12)). A similar decomposition has now been performed into V, A_p and A_f terms, given in figure 17(*b*). With three terms contributing to F_t', three primary and two cross-correlation terms appear. In normalized form, the contributions to α_t can be written as

$$1 = V^2 + A^2 + 2H^2 + 2HV + 2HA \tag{4.24}$$

with V^2 the velocity or unsteady drag force group, and A the pressure and H the friction force acceleration terms. HV and HA indicate the two cross-correlation terms.

Figure 17(*b*) shows that at low Re_ω the total unsteady force is dominated by V^2, with HV contributing most of the remainder. All terms are greater than zero and the terms HV and HA do not counteract V^2, A^2 or H^2. The individual contributions of A^2 and H^2 as well as their cross-correlation are negligible in this regime, while the large value of HV arises due to the large value of V.

At higher Re_ω, A^2 increases monotonically while V^2 decreases. All other terms exhibit intermediate maxima. Although $(1 - R_p)A_f$ increases monotonically with Re_ω (figure 17*a*) its relative contribution H^2 reaches an intermediate maximum and decays to high Re_ω. Furthermore, while the amplitude $(1 - R_p)A_f$ remains below R_pA_p, its contribution in both H^2 and in HV is larger than A^2 over a considerable range of Re_ω. Only in the high Re_ω range does A^2 become the dominant term, together with HA. This decomposition shows clearly that there is no basis on which to neglect the effect of the history force and only retain the added mass force when trying to model the behaviour of unsteady forces.

5. Summary and conclusion

In this paper we have examined in detail the unsteady flow and forces associated with oscillatory fluid flow in SCL arrays of spheres. The fluid flow through these fixed beds was simulated using the lattice-Boltzmann method. Unsteady flow conditions were obtained by applying a small-amplitude oscillation to the body force that drives the flow. Simulations have been done for a range of particle volume fractions (ϕ), background flow Reynolds numbers (Re_p) and oscillatory flow Reynolds numbers (Re_ω).

Much work has been reported in the literature on unsteady forces acting on isolated particles and on assemblies of particles in the limit of very high Re_ω values. In latter context the Stokes boundary layers on various particles do not overlap with each other, while in the former case there is no second particle to interfere with the Stokes boundary layer of the test particle. In our work on flow through particle assemblies, we have considered both small and high values of Re_ω where interaction between the Stokes boundary layers on neighboring particles occur and do not occur, respectively. When Stokes boundary layer interaction occurs, the response of the unsteady flow field differs quantitatively from that predicted by an unsteady Stokes flow analysis which neglects this interaction (e.g. see figures 6 and 7).

It is known that for isolated spheres the virtual mass force contributes to the pressure force only and obtains the regular coefficient of 0.5 (Rivero *et al.* 1991; Mei *et al.* 1991; Mei & Adrian 1992; Chang & Maxey 1994; Kim *et al.* 1998). We found that at high Re_ω the phase angles of the pressure and friction forces in the periodic arrays approach those of the virtual mass and history forces for isolated spheres (figure 13). Therefore, a decomposition where the virtual mass force only contributes to the pressure force and the history force only contributes to the friction force appears reasonable and has been taken as the basis of our analysis of unsteady forces. While the term virtual mass is reserved for inviscid flow, in our analysis over a range of flow conditions inevitably viscous contributions to the pressure force will be present. Hence the term apparent virtual mass is used to indicate the accelerative part of the pressure force.

Our analysis of the unsteady forces revealed several features:

(*a*) At low Re_p values and in the limit $Re_\omega \to 0$, the quasi-steady-state drag force extracted from the simulations approached the steady-state drag force results (figure 9). At increasing Re_p the quasi-steady-state drag force was shown to increase more

strongly than the steady-state drag force (figure 11), similar to the observations of Mei *et al.* (1991) for isolated spheres.

(*b*) The unsteady drag coefficient varies with Re_ω (figure 17) even in the case of low Re_p; the contributions of the pressure and friction force components to the unsteady drag coefficient are brought out in this study (figures 16*b* and 16*d*).

(*c*) The strong decay of the history force towards low Re_ω that has been reported previously for isolated spheres by Mei *et al.* (1991) is also observed in the current simulations. For isolated spheres this strong decay was associated with the interaction between the Stokes boundary layer and advection in the Oseen region of the flow field. In our simulations, where the limited space between the particles causes interaction between the Stokes boundary layers attached to neighbouring particles, the decay of the history force occurs at higher Re_ω values than for isolated spheres.

(*d*) The slope of the acceleration term in the pressure force, which is comparable to the virtual mass coefficient, was found to depend on Re_ω. This should be contrasted with the finding of Mei *et al.* (1991) for isolated spheres that the apparent virtual mass coefficient was 0.5 and independent of Re_ω. The different behaviour observed in our simulations is shown to be linked to the interaction between the Stokes boundary layers; when little interaction occurs, at high Re_ω, the apparent virtual mass coefficient was found to approach 0.5, while in the presence of interaction, at lower Re_ω, it rises to 1.0.

The present study focused on the effect of unsteady flow on the forces acting on steady, non-moving particles in an SCL arrangement. We limited ourselves to this geometry mainly for computational efficiency. We also carried out a small number of simulations in FCC geometry and found that the trends in the data on the FCC geometry simulations were qualitatively identical to the SCL type simulations. These results were therefore not further discussed in this manuscript.

If the particles are free to move, the complexity of the problem increases significantly; for instance, the particle Stokes number comes into play through the particle density and the particle arrangement in unsteady clusters of particles will be very different from that in ordered arrays. Although our current study ignores these additional complexities, it still allows us to make some observations on the use of unsteady interphase interaction force models in two-fluid simulations. The easiest and most common approach is to apply a closure that only addresses the (quasi-steady-state) drag force, while a second straightforward extension is to impose a virtual mass term with a virtual mass coefficient of 0.5. The present study has shown that for highly unsteady flows a virtual mass coefficient of 0.5 is a reasonable estimate in high-Re_ω conditions (prevailing, for example, in turbulent suspension flows); however, in this regime, the apparent virtual mass force accounts only for $\sim$50% of the total unsteady force (figure 17). The contribution of the history force and the history–apparent virtual mass force correlation can be of the same order of magnitude or larger. Therefore, in a two-fluid model analysis of fluid–particle flows, if the virtual mass force term is estimated to be significant, the chances are that the history force term is also important.

This work was supported by a grant from the New Jersey Commission on Science and Technology.

REFERENCES

Artoli, A., Hoekstra, A. G. & Sloot, P. 2002 3d pulsatile flow with the lattice Boltzmann BGK method. *Intl J. Mod. Phys.* C **13**, 1119–1134.

Bagchi, P. & Balachandar, S. 2003 Inertial and viscous forces on a rigid sphere in straining flows at moderate Reynolds numbers. *J. Fluid Mech.* **481**, 105–148.

Basset, A. B. 1888 *A Treatise in Hydrodynamics*. Deighton, Bell, and Co.

Biesheuvel, A. & Spoelstra, S. 1989 The added mass coefficient of a dispersion of spherical gas bubbles in liquid. *Intl J. Multiphase Flow* **15**, 911–924.

Chang, E. J. & Maxey, M. R. 1994 Unsteady flow about a sphere at low to moderate Reynolds number. Part 1. Oscillatory motion. *J. Fluid Mech.* **277**, 347–379.

Chang, E. J. & Maxey, M. R. 1995 Unsteady flow about a sphere at low to moderate Reynolds number. Part 2. Accelerated motion. *J. Fluid Mech.* **303**, 133–153.

Chen, S. & Doolen, G. D. 1998 Lattice Boltzmann method for fluid flows. *Annu. Rev. Fluid Mech.* **30**, 329–364.

Chopard, B. & Droz, M. 1998 *Cellular Automata Modeling of Physical Systems*, 1st Edn. Cambridge University Press.

Clift, R., Grace, J. R. & Weber, M. E. 1978 *Bubbles, Drops and Particles*. Academic.

Crowe, C., Sommerfeld, M. & Tsuji, Y. 1997 *Multiphase Flows with Droplets and Particles*, 1st Edn. CRC Press.

Felderhof, B. U. 1991 Virtual mass and drag in two-phase flow. *J. Fluid Mech.* **225**, 177–196.

Hasimoto, H. 1959 On the periodic fundamental solutions of the Stokes equations and their application to viscous flow past a cubic array of spheres. *J. Fluid Mech.* **5**, 317–328.

Hill, R. J., Koch, D. L. & Ladd, A. J. C. 2001*a* The first effects of fluid inertia on flows in ordered and random arrays of spheres. *J. Fluid Mech.* **448**, 213–241.

Hill, R. J., Koch, D. L. & Ladd, A. J. C. 2001*b* Moderate-Reynolds-number flows in ordered and random arrays of spheres. *J. Fluid Mech.* **448**, 243–278.

Jackson, R. 2000 *The Dynamics of Fluidized Particles*, 1st Edn. Cambridge University Press.

Kandhai, D., Derksen, J. J. & Van den Akker, H. E. A. 2003 Interphase drag coefficients in gas-solid flows. *AIChE J.* **49**, 1060–1065.

Kim, I., Elghobashi, S. & Sirignano, W. A. 1998 On the equation for spherical-particle motion: effect of Reynolds and acceleration numbers. *J. Fluid Mech.* **367**, 221–253.

Ladd, A. J. C. 1994 Numerical simulations of particulate suspensions via a discretized Boltzmann equation. Part 1. Theoretical foundation. *J. Fluid Mech.* **271**, 285–309.

Landau, L. D. & Lifshitz, E. M. 1978 *Fluid Mechanics*, 1st Edn. Pergamon.

Li, J. & Kuipers, J. A. M. 2003 Gas-particle interactions in dense gas-fluidized beds. *Chem. Engng Sci.* **58**, 711–718.

Lovalenti, P. M. & Brady, J. F. 1993*a* The hydrodynamic force on a rigid particle undergoing arbitrary time-dependent motin at small reynolds number. *J. Fluid Mech.* **256**, 561–605.

Lovalenti, P. M. & Brady, J. F. 1993*b* The force on a sphere in a uniform flow with small-amplitude oscillations at finite Reynolds number. *J. Fluid Mech.* **256**, 607–614.

Mei, R. 1994 Flow due to an oscillating sphere and an expression for unsteady drag on the sphere at finite Reynolds number. *J. Fluid Mech.* **270**, 133–174.

Mei, R. & Adrian, R. J. 1992 Flow past a sphere with an oscillation in the free-stream velocity and unsteady drag at finite Reynolds number. *J. Fluid Mech.* **237**, 323–341.

Mei, R., Lawrence, C. J. & Adrian, R. J. 1991 Unsteady drag on a sphere at finite Reynolds number with small fluctuations in the free-stream velocity. *J. Fluid Mech.* **233**, 613–631.

Odar, F. & Hamilton, W. S. 1964 Forces on a sphere accelerating in a viscous fluid. *J. Fluid Mech.* **18**, 302–314.

Odar, F. & Hamilton, W. S. 1966 Verification of the proposed equation for calculation of the forces on a sphere accelerating in a viscous fluid. *J. Fluid Mech.* **25**, 591–592.

Pozrikidis, C. 1997 *Introduction to Theoretical and Computational Fluid Dynamics*, 1st Edn. Oxford University Press.

Qian, Y., d'Humieres, D. & Lallemand, P. 1992 Lattice BGK models for Navier–Stokes equation. *Europhys. Lett.* **17**, 479–484.

Rivero, M., Magnaudet, J. & Fabre, J. 1991 Quelques résultats nouveaux concernant les forces exercées sur une inclusion sphérique par un écoulement accéléré. *C.R. Acad. Sci. Paris* II **312**, 1499–1506.

Rothman, D. H. & Zaleski, S. 1997 *Lattice-Gas Cellular Automata*, 1st Edn. Cambridge University Press.

Sangani, A. S. & Acrivos, A. 1982 Slow flow through a periodic array of spheres. *Intl J. Multiphase Flow* **8**, 343–360.

Sangani, A. S., Zhang, D. Z. & Prosperetti, A. 1991 The added mass, basset- and viscous drag coefficients in nondilute bubbly liquids undergoing small-amplitude oscillatory motion. *Phys. Fluids* A **3**, 2955–2970.

Schöneborn, P.-R. 1975 The interaction between a single particle and an oscillating fluid. *Intl J. Multiphase Flow* **2**, 307–317.

Stephanopoulos, G. 1984 *Chemical Process Control: An Introduction to Theory and Practice*, 1st Edn. Prentice-Hall.

Succi, S. 2001 *The Lattice Boltzmann Equation for Fluid Dynamics and Beyond*, 1st Edn. Oxford University Press.

Zuber, N. 1964 On the dispersed two-phase flow in the laminar flow regime. *Chem. Engng Sci.* **19**, 897–917.